THESIS FOR THE DEGREE OF LICENTIATE OF ENGINEERING

Characterization of biological nanoparticles using evanescent field sensing

MATTIAS SJÖBERG

CHALMERS
UNIVERSITY OF TECHNOLOGY

Department of Physics
CHALMERS UNIVERSITY OF TECHNOLOGY
Gothenburg, Sweden 2020

Characterization of biological nanoparticles using evanescent field sensing

MATTIAS SJÖBERG

Department of Physics
Chalmers University of Technology
SE-412 96 Göteborg
Sweden
Telephone +46(0)31-772 10 00

Printed at Chalmers Reproservice
Göteborg, 2020

Cover illustration: *Conceptual illustration of a lipid vesicle coated with a protein film, located above a surface exhibiting an evanescent illumination field.*

Characterization of biological nanoparticles using evanescent field sensing

MATTIAS SJÖBERG

Department of Physics
Chalmers University of Technology
Göteborg, Sweden 2020

Abstract

In light of the increasingly realized importance of nanoparticle-based biological processes, in biology as well as in technological applications, there is a need of analysis methods capable of accurately quantifying different characteristics and processes involving these elusive entities. The aim of this thesis is the development and utilization of surface-based bioanalytical sensing methods for quantitative characterization of biological nanoparticles, most of which being based on surface-confined evanescent-field illumination. The possibility to use waveguide-based evanescent scattering microscopy for quantitative analysis of protein binding to nanoparticles has been investigated through observation of binding of streptavidin and antibodies to biotinylated liposomes. This system was additionally investigated using a range of complementary measurement approaches, including nanoparticle tracking analysis, conventional and localized surface plasmon resonance sensing, and quartz crystal microbalance with dissipation monitoring. It was concluded that the waveguide microscopy method provides quantitative information in good agreement with established methods, but offers certain key advantages, such as the possibility to provide single-particle resolved label-free information on protein binding kinetics combined with the possibility of simultaneous total internal reflection fluorescence microscopy measurements. In addition, dual-wavelength surface plasmon resonance sensing was used to investigate how the lipid phase characteristics of liposomes affect their behaviour in relation to multivalent interactions with a supported lipid bilayer. This system mimics the initial processes of cellular uptake. Specifically, the interplay between lipid phase (i.e. gel or fluid), interaction valency and liposome deformation was studied. It was demonstrated that fluid-phase liposomes are more prone to deform than their gel-phase counterparts, and that the degree of deformation depends on the number of ligand-receptor pairs engaged in the binding.

Keywords: Waveguide scattering microscopy, SPR, liposomes, protein corona, label-free, single-particle, mass quantification.

Appended papers

The papers appended in this thesis are listed below. The papers are referred to using their roman numerals through-out the thesis.

Paper I:

Time-Resolved and Label-Free Evanescent-Light-Scattering Microscopy offers Mass Quantification upon Protein Binding to Single Lipid-Vesicles

Mattias Sjöberg, Björn Agnarsson, Antonius Armanious, Mokhtar Mapar, Vladimir P. Zhdanov, and Fredrik Höök.

In manuscript.

My contribution: I was responsible for the design and planning of the experiments. I performed the experiments and data analysis, and wrote the manuscript.

Paper II:

Differential Deformation of Fluid and Gel Phase Liposomes upon Multivalent Interaction with Cell Membrane Mimics Revealed using Dual Wavelength Surface Plasmon Resonance

Karin Norling, Mattias Sjöberg, Marta Bally, Vladimir Zhdanov, Nagma Parveen, Fredrik Höök

In manuscript.

My contribution: I performed some of the surface plasmon resonance measurements, partook in the data analysis and wrote parts of the manuscript.

Publications not included in the thesis

Paper III:

Low-temperature fabrication and characterization of a symmetric hybrid organic–inorganic slab waveguide for evanescent light microscopy

Björn Agnarsson, Mokhtar Mapar, Mattias Sjöberg, Mohammadreza Alizadehheidari and Fredrik Höök

Nano Futures **2** (2018).

Contents

List of abbreviations

- **BNP** - Biological nanoparticle
- **CMOS** - Complementary metal oxide semiconductor
- **DNA** - Deoxyribonucleic acid
- **DOPC** - 1,2-dioleoyl-sn-glycero-3-phosphocholine
- **DOPE** - 1,2-dioleoyl-sn-glycero-3-phosphoethanolamine
- **DSPE** - 1,2-distearoyl-sn-glycero-3-phosphoethanolamine
- **IgG** - Immunoglobulin G
- **LSPR** - Localized surface plasmon resonance
- **PBS** - Phosphate buffered saline
- **PEG** - poly(ethylene glycol)
- **POPC** - 1-palmitoyl-2-oleoyl-sn-glycero-3-phosphocholine
- **QCM-D** - Quartz crystal microbalance with dissipation monitoring
- **RNA** - Ribonucleic acid
- **SLB** - Supported lipid bilayer
- **SPR** - Surface plasmon resonance
- **TIRFM** - Total internal reflection fluorescence microscopy

1

Introduction

"The light of the body is the eye: if therefore thine eye be sound, thy whole body shall be full of light."

— Matt 6:22

As a sound eye illuminates the whole body, sound microscopy brings light and understanding to biophysical phenomena with an intuitive touch the like of which is otherwise rather elusive. The saying *"to see is to believe"* has perhaps never been as potently manifested as with the publication and wide spread of Robert Hooke's *Micrographia* in 1665[1], rich with illustrations of his microscopy observations of various biological structures in detail thitherto unseen and in which he coined the biological term *cell*. In the plethora of available instrumentation for investigating biological systems, generation of data in the form of images, as is possible with microscopy, often offers a shortcut to intuitive understanding and has since its introduction remained a central component in the scientific investigation of biological systems[2].

What cannot be seen does, however, require the use of complementary approaches; a fact not overlooked by researchers, especially of the last few decades, which have in an impressive collaborative effort brought forth a multitude of various biosensing technologies with the aim of usage in a range of fields of immense societal importance such as diagnostics, drug development and fundamental biophysical research[3].

The work you are currently reading has in its core motivation questions on the nature and potential applicability of biological nanoparticles (BNPs)[4], entities with dimensions $\lesssim 100\,\mathrm{nm}$ consisting of biological or biocompatible materials, and aims at an answering approach through investigations of lipid vesicles. In a general sense, increased understanding of biological nanoparticles brings with it potential for novel developments in prevention and treatment of disease[5]. An illustrative example is the history of humanities comprehension of extracellular vesicles. After initially being considered cellular debris awakening limited interest, these BNPs were eventually identified as important carriers of genetic, proteinaceous and lipidic material[6, 7] which consequently initiated a surge in method development and associated studies[8]. Comprehension of the role of extracellular vesicles

thus open the door to this biological mechanism as a novel target for affecting the state of cells and their associated response, an effort constituting the principle of many drugs.

Extracellular vesicles as well as other objects in this size range (both native and artificial, organic and inorganic) are of current interest in the context of drug delivery[9, 10]. Nanoparticles have started to be used for the highly sought-after goal of site-specific transmembranal delivery of otherwise immunogenic entities[11, 12]. This includes e.g. cyclodextrin polymer nanoparticles[13] as well as lipid nanoparticles for RNA delivery[14].

Successful design and choice of novel nanoparticle-based delivery systems hinges upon a number of questions, many of which relates to *surface interactions*, both in the context of entities interacting with the surface of nanoparticles (paper I) and in the context of nanoparticles interacting with other surfaces (paper II), not least the surfaces of their intended target, often being the cytoplasmic membrane. A major topic of the former context is that of protein corona formation[15] while the latter relates to, for example, transmembranal delivery through polyvalent interactions[11, 16, 17].

This thesis concerns the development of an approach to the investigation of properties of biological nanoparticles with the aim of, through the combination of various methods and their conjunction, painting a picture dense with information, a picture more revealing than achievable through any individual method alone. A conglomerate greater than the sum of its parts. This assortment includes the direct use of light for generation of images through *waveguide microscopy*, the indirect use of light by laser induced *surface plasmon resonance sensing* (SPR) and other methods such as the *quartz crystal microbalance with dissipation* (QCM-D) *monitoring* technique. The above sensing approaches all fall under the category of *surface sensing methods*, technologies for studying entities close to or interacting with a sensor surface.

The work presented in this thesis is summarized in two soon-to-be published scientific papers. Paper I concerns the investigation of protein binding to biotinylated lipid vesicles through waveguide microscopy as a means to study particles at an individual level, combined with SPR and QCM-D, which provides additional information at an ensemble average level. The waveguide microscopy method provides the opportunity to simultaneously observe light emitted from fluorescently labelled proteins and changes in light scattering, and thus independent of labels, from the vesicles. It is shown that label-free single-particle-resolved scattering microscopy provides quantitative data interpretable as mass of a film formed on the outer surface of the vesicles, with values in good agreement with those obtained from the complementary ensemble average measurements. The nature of the scattering data, with the potential of simultaneous observation of a multitude of individual particles, allows for data ensemble averaging comparable to the other methods but with the benefit of active background exclusion.

Surface plasmon resonance sensing provides data on changes of refractive index near a sensor surface, which can be utilized for studying surface bound nanoparticles in terms of adsorbed mass and sample dimensions. Both papers I and II use dual-wavelength SPR

measurements for this purpose, analyzing mass of proteins bound to vesicles and thereof imparted structural changes as well as potential deformation of vesicles due to interactions with an underlying supported lipid bilayer and target proteins therein. Paper II specifically focuses on liposomal deformation upon polyvalent interaction with proteins bound to a cell membrane mimic and how this relates to the phase behavior of the liposome lipid bilayer. It is shown that this method offers the possibility of investigating and potentially disentangling the effects of nanoparticle deformation and interaction valency and that differences in deformability seems to play an important role in this cellular uptake-related process.

This thesis will begin with two chapters describing the foundation of the project in terms of its biological and theoretical background. The next chapter discusses the experimental methods utilized in this work after which a chapter summarizing the two appended papers follows. The thesis ends with a discussion on possible future routes for the project.

2

Biological background

"Var dag den första —. Var dag ett liv."
— Dag Hammarskjöld

The increasing fundamental understanding of life, its building blocks and the biophysical processes it involves has been accompanied by the development of successively more effective approaches and technology for treatment of disease. The vast route from humourism-inspired treatments[1], through the advent of germ theory and bacteriology all the way to the achievements of modern medicine has been marked by successively more revealing technologies.

The advent of nanotechnology in its modern understanding, methods concerning the size range $\lesssim 100\,\mathrm{nm}$, brought with it the possibility of harnessing or mimicking a vast array of biological processes at this scale, which includes a range of important cellular communication pathways[19]. A significant part of this is the use of nanoparticles. Particles which fall under this broad category and have been applied in biotechnology include artificially produced organic and inorganic particles such as metal–organic framework-based[20] or silica-based[21] particles as well as particles already present in biological systems such as viruses, exosomes and (extra- and intracellular) vesicles[22–26].

A major purpose of biologically native nanoparticles is that of delivery, the internal transportation of vital cargo[27]. As discussed in the previous section, an important subset of these consists of extracellular vesicles which are believed to play an important role in a significant number of physical processes. Another important category in this context is that of viruses, particles which through oligonucleotide delivery into the intracellular machinery self-replicate and have a large impact on our lives, sometimes causing problems of world-wide magnitude[2]. One of the main properties of interest of these BNPs in

[1] The outdated and misguided theory, with ancient roots, that health is governed by the internal balance of a number of fluids, or humors. Practices based on this idea, such as bloodletting, lasted well into the 1800s and the emergence of modern medicine[18].

[2] A fact currently more evident than in living memory. As I write these words, a large part of the world is in lockdown due to the COVID-19 pandemic.

the context of biomimicry and medical applications is that of site-specific transmembranal delivery[28] of otherwise immunogenic entities. This includes the so-called *high-molecular weight drugs*, which has come to constitute an increasing part of current medical research efforts[12, 29, 30].

Of great importance for the development and utilization of BNPs for technological applications is access to tools for investigating the properties which determine their function. A current gap in this method assortment are tools for properly understanding the modes of interaction between particles and their environment, which in this context often consists of complex aqueous solutions of biological materials and in vivo interfaces such as the cytoplasmic membrane.

This thesis consists of implementation and investigation of tools for this purpose, which in the proof-of-principle studies conducted so far have been used for studying artificially produced lipid vesicles in the $\sim 100\,\mathrm{nm}$ size range, chosen both for their inherent interesting physicochemical properties but also for their role as models of their more complex counterparts discussed above.

The following section provides a basic review of lipidic structures of relevance to this work, including lipid vesicles, followed by a brief introduction to other biological concepts of particular interest.

2.1 Lipids, membranes and vesicles

Lipids is a loosely defined term for a category of biomolecules solvable in non-polar solvents, whose biological function includes energy storage, signaling and to act as structural components of the cytosolic membrane[31]. The latter function is fulfilled mainly by the subset called *phospholipids* which generally consists of two hydrophobic fatty acid tails and a hydrophilic phosphate head-group, linked through a glycerol backbone (see figure 2.1). The dual nature of the phospholipid components makes phospholipids *amphiphilic*, which means that while the headgroup can incorporate into the hydrogen bond network present in polar solutions such as water, the tails cannot. The entropic consequences of this fact causes a variety of lipidic structures to spontaneously form upon placing phospholipids in an aqueous environment, the apparent purpose of which is to hide the hydrophobic tails from the polar water molecules, usually by arrangements directing the tails against each other. Depending on a range of variables including physicochemical properties of the lipids and their environment these structures include micellar and bilayer enclosed vesicle particles of various shapes, sizes and lamellarity[3], as well as surface associated structures such as the supported lipid bilayer (SLB) (see figure 2.2)[31, 32].

One of many purposes of lipids is to form the cytosolic membrane, or *cell membrane*, which makes up an essential component of life as we know it. By constituting a hydropho-

[3]Consisting of one (monolamellar) or multiple (multilamellar) bilayers. A multilamellar vesicle can thus be seen as multiple mutually concentrically enclosing vesicles.

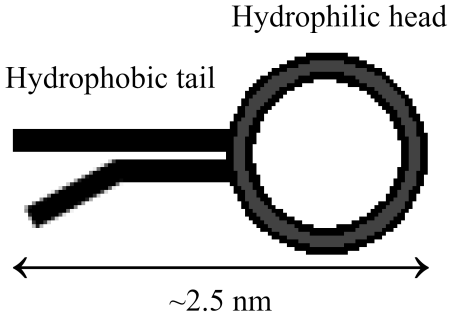

Figure 2.1: Illustration of a phospholipid, consistin of a two hydrophobic fatty acid tails and a hydrophilic phosphate group containing head.

bic barrier through which different molecules and ions can be selectively translocated, the membrane allows for biological systems to be compartmentalized into regions of vastly different chemical conditions, e.g. cells and some of their indwelling organelles. The contrasts between these different compartments is of crucial importance for a multitude of biological activities. The cell membrane is highly complex both in its varying compositions and in its varying states which in turn depend on environmental factors. In many cases it can be considered a two-dimensional fluid, in which the components such as lipids and membrane proteins diffuse, forming both permanent and transient structures[27]. It is, however, possible to induce phase shifts, where a transition from a fluid to a gel phase occurs, significantly reducing the component mobility[33]. These different vesicle membrane phases and their consequences for interactions with a model cell membrane is investigated in paper II. More specifically, the interplay between interaction valency (i.e. number of ligand-receptor bonds) and vesicle rigidity (which varies with lipid phase) is investigated. Vesicles of different phase but with equal number of receptors are observed during interaction with ligand-functionalized SLBs (see figure 2.3 for an overview and section 5.2 for more details).

Many studies, including those presented here, models the cell membrane and native lipidic structures through systems consisting of a limited number of chosen components in order to reduce complexity and disentangle specific properties and effects of interest. In this work lipid vesicles and supported lipid membranes consisting of various combinations of the lipids denoted POPC, DOPC, DSPC and DSPE were used (see figure 2.4 for a structural formula example). The latter with the headgroup conjugated to a polyethylene glycol (PEG)-biotin group to allow for selective binding of biotin-compatible compounds.

Paper I additionally utilizes the concept of DNA-tethers for binding vesicles to the underlying surface. These 30 basepairs long double-stranded polymers are in one end biotinylated and in the other cholesterolated, which respectively can be utilized for binding to streptavidin and self-incorporating into a lipid bilayer[34].

Artificial vesicles as used in this work are made using established protocols[35]. The basic

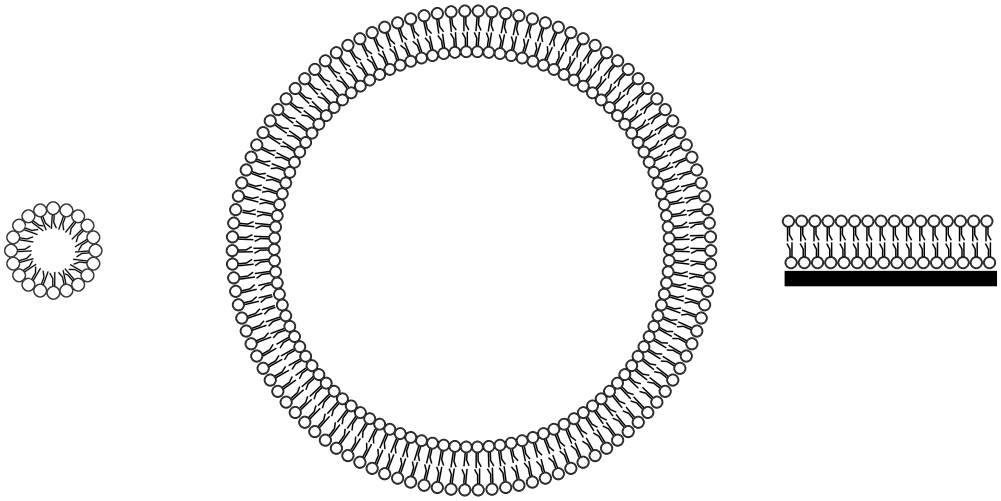

Figure 2.2: Two-dimensional illustrations of lipidic structures in the form of, from left to right: A micelle, a monolamellar vesicle and a supported lipid bilayer.

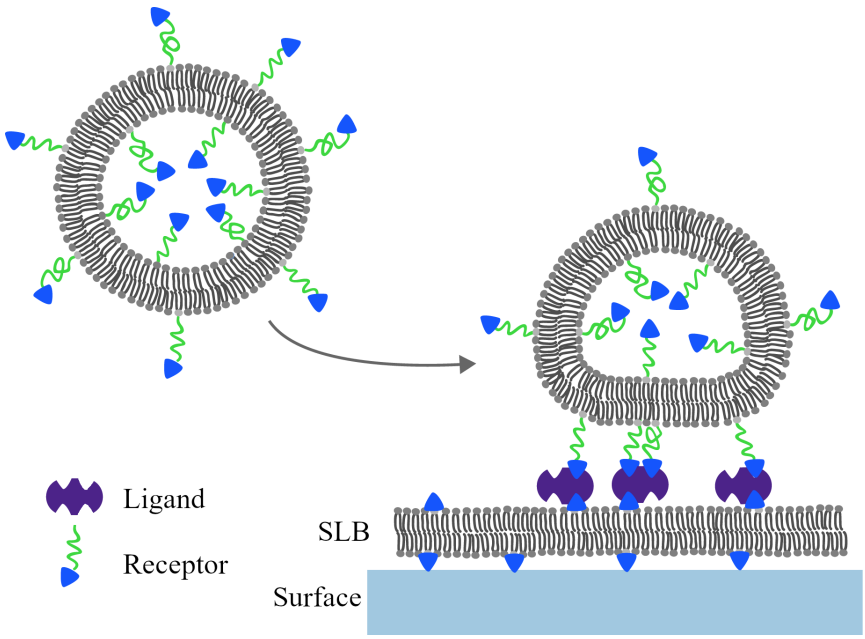

Figure 2.3: Illustration of the system under investigation in paper II. Vesicles containing receptors interact with ligands on an underlying supported lipid bilayer which causes vesicle deformation. The dependence of vesicle deformation on the vesicle lipid phase and the number of available ligands is investigated by measuring the vertical dimensions of the system (i.e. the height).

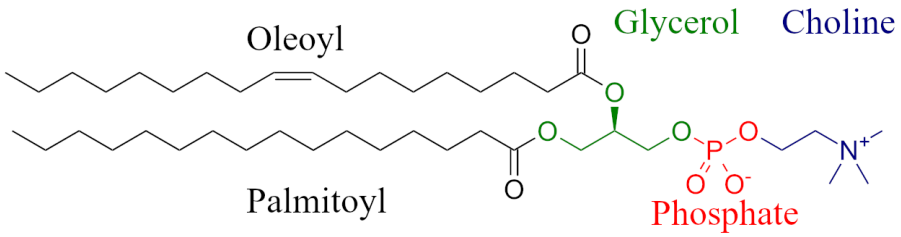

Figure 2.4: The chemical structural formula of 1-palmitoyl-2oleoyl-sn-glycero-3phosphocholine, abbreviated as POPC, serving here as an example of the structure of a phospholipid. The different parts are labelled for clarity.

idea consists of generating a dry film of lipids that is subsequently hydrated, leading to the creation of vesicles of various sizes and lamellarity. As a homogeneous sample of narrow size distribution and monolamellarity is desired, the vesicles are freeze-thawed, i.e. alternatingly frozen in liquid nitrogen and thawed in a warm water bath, and extruded, repeatedly pressed through a polycarbonate membrane with a defined pore size. This produces a vesicle solution of relatively homogeneous size distribution and lamellarity[36].

2.2 The protein corona

Upon exposure to a complex biological solution, nanoparticles are with few exceptions, rapidly covered by a dense layer of biomolecular compounds, often referred to as the *protein corona*[37]. Spoken of in this very general sense this, usually a few nm thick[38], dynamic biofilm contains a subset of approximately 100-200 proteins, of which immunoglobulin G, serum albumin, fibrinogen, clusterin and apolipoproteins are especially common, as well as other biomolecules such as nucleic acids, sugars and lipids[39–41]. The exact composition of a protein corona is expected to depend on a range of parameters including nanoparticle material, size, shape, charge and environmental factors such as solution composition, temperature and pH[37]. This complex variety of adherents severely complicates the utilization of BNPs for medical purposes since their actual surfaces in vivo often differ significantly from what is envisioned in their design and preparation, where certain interactions with a target interface is desired. There is indeed increasing evidence for a both spatially and temporarily diverse corona e.g. the low affinity-high exchange rate *soft* and the high affinity-low exchange rate *hard* corona[42], the properties of which are far from properly understood from an application perspective. Methods for qualitative and quantitative investigation of protein binding and interaction with nanoparticle surfaces is thus an important key to improved understanding and applicability of practical usage of nanoparticles in vivo. The focus of paper I is to provide a new means to explore protein corona formation on (biological) nanoparticles.

Questions relating to the protein corona have been addressed with a wide range of methods,

including ensemble average methods such as dynamic light scattering[43], mass-spectrometry[44, 45] and surface sensitive methods like the quartz crystal microbalance (QCM)[46] and surface plasmon resonance (SPR) sensing[47, 48] as well as methods with single nanoparticle resolution such as electron microscopy[43] and flow cytometry[49]. Together, these methods offer multiparametric information with respect to protein coverage and identity, changes in NP size as well as corona-induced structural changes. Despite this fairly broad assortment of analytical methods, there is still a pronounced gap with respect to reliable methods capable of investigating the dynamics of protein-corona formation with single nanoparticle resolution, label-free readout and quantitative determination of changes in biomolecular mass.

In order to develop such a method, a system of biotinylated vesicles (as described in the previous section) served as model nanoparticles to which the proteins *streptavidin* and *anti-biotin IgG* were bound under observation. Streptavidin is a 52.8 kDa tetrameric protein, in many ways similar to Avidin, and exhibits in its affinity to biotin one of the strongest non-covalent binding interactions known in nature[50]. Anti-biotin is an immunoglobulin G antibody, of 150 kDa, binding to biotin as well. These two chosen proteins differ in size and affinity and thus provides different experimental conditions to explore in the measurements performed.

3

Theoretical background

"As long as you are content with walks on the beach, your own glimpses are far more fun than looking at a map [of the Atlantic]. But the map is going to be more use than walks on the beach if you want to get to America."

— C.S Lewis

EXPERIMENTS SANS THEORY tend to suffer from imprecision and excessive heuristics while theory without experiments risks ambling into the realm of speculation. In some fields of physics necessity dictates the need to live in one of these extremities, and there is undeniable value and beauty there, but physics in its most satisfactory manifestations combines both aspects in a mutually reinforcing interplay. This thesis is in essence based on experimental work, but prior to discussing methodology, a theoretical foundation must be lain.

3.1 Traveling light through optical theory

At the heart of this thesis lies a number of experimental methods whose operational principles relate to the nature of light-matter interactions. Although a full discussion on the rather intricate theoretical foundations of these phenomena is beyond the scope of this text it is both necessary and illuminating to meander through optical theory with a number of sojourns to pick up the ideas of most relevance and applicability with respect to this work. For the reader desiring more extensive theory there is a multitude of excellent literature on the subject. If you seek intuitive understanding, read Feynman[51]. For rigor, read Hecht[52, 53] and Bohren & Huffman[54].

Discussions on the nature of light tend to start with the Maxwell equations, so here as well. These are often expressed as a set of coupled partial differential equations and describe the macroscopic generation and temporal evolution of electromagnetic fields. They can be expressed as follows:

$$\nabla \cdot \boldsymbol{E} = \frac{\rho}{\varepsilon} \tag{3.1}$$

$$\nabla \cdot \boldsymbol{B} = 0 \tag{3.2}$$

$$\nabla \times \boldsymbol{E} = -\frac{\partial B}{\partial t} \tag{3.3}$$

$$\nabla \times \boldsymbol{B} = \mu\Big(\boldsymbol{J} + \varepsilon\frac{\partial \boldsymbol{E}}{\partial t}\Big) \tag{3.4}$$

Here, $\boldsymbol{E}$ is the electric field, $\boldsymbol{B}$ the magnetic field, $\boldsymbol{J}$ the electric current density, ρ the free charge density, t time, $\varepsilon = \varepsilon_0\varepsilon_r$ the permittivity and $\mu = \mu_0\mu_r$ the permeability. ε_0 and μ_0 are the electric and magnetic constants and ε_r and μ_r the relative permittivity and permeability. $\boldsymbol{J}$ relates to electrical conductivity, σ, as $\boldsymbol{J} = \sigma\boldsymbol{E}$.

These four equations, in conjunction with the Lorentz force law, which describes the electromagnetic force $\boldsymbol{F}$ exerted on a point charge of charge q and velocity $\boldsymbol{v}$:

$$\boldsymbol{F} = q(\boldsymbol{E} + \boldsymbol{v} \times \boldsymbol{B}), \tag{3.5}$$

forms the foundation of classical electromagnetic theory.

A consequence of the nature of the electromagnetic fields, as became evident with the formulation of the Maxwell equations, is the possibility and existence of self-perpetuating electromagnetic waves; a varying electric field will generate a magnetic field and vice versa. Hidden in this system of equations one can thus suspect the presence of a wave equation, which is indeed the case. In free space, in the absence of sources and currents (i.e $\rho = \boldsymbol{J} = 0$) taking the curl of equation (3.3) and utilizing the vector identity $\nabla \times (\nabla \times \boldsymbol{E}) = \nabla(\nabla \cdot \boldsymbol{E}) - \nabla^2\boldsymbol{E}$ results in a homogeneous wave equation:

$$\nabla^2\boldsymbol{E} = \varepsilon\mu\frac{\partial^2\boldsymbol{E}}{\partial t^2} \tag{3.6}$$

This equation describes an electromagnetic wave propagating in space with the phase velocity $1/\sqrt{\varepsilon\mu}$. One of the remarkable discoveries of Maxwell as he formulated these equations is that ε and μ, constants describing the electromagnetic field properties in specific media, combined this way coincided precisely with the experimentally determined speed of light, $c = 1/\sqrt{\varepsilon\mu}$. The important conclusion was that light itself is in fact an electromagnetic wave. Two physical phenomena, previously considered separate, had been elegantly unified.

A well known set of solutions to the Maxwell equations which satisfies the wave equation and from which, through superposition, all other solutions can be formed, are plane waves[52]:

$$\boldsymbol{E} = \boldsymbol{E}_0 e^{-i\boldsymbol{k}\cdot\boldsymbol{x} - i\omega t} \tag{3.7}$$

where ω is the field angular frequency and $|\boldsymbol{E}| = E_0$ is the amplitude and $\boldsymbol{k} = \boldsymbol{k'} + i\boldsymbol{k''}$ is the complex wave vector which describes the wave spatial frequency, direction of propagation and attenuation.

Analogue to the above reasoning the magnetic field can be similarly expressed as:

$$\boldsymbol{B} = \boldsymbol{B}_0 e^{-i\boldsymbol{k}\cdot\boldsymbol{x} - i\omega t} \tag{3.8}$$

Considering the equations (3.3) and (3.4) for this plane wave gives:

$$\boldsymbol{k} \times \boldsymbol{E}_0 = \omega \boldsymbol{B}_0 \tag{3.9}$$

$$\boldsymbol{k} \times \boldsymbol{B}_0 = -\omega\varepsilon\mu \boldsymbol{E}_0 \tag{3.10}$$

These equations reveal the fact that electromagnetic radiation consists of an electric and a magnetic field, both perpendicular to each other as well as to the direction of propagation $\boldsymbol{k}/|\boldsymbol{k}|$.

The plane wave solutions additionally allow the reformulation of the wave equation (3.6) as:

$$\nabla^2 \boldsymbol{E} + \varepsilon\mu\omega^2 \boldsymbol{E} = 0 \tag{3.11}$$

or

$$\nabla^2 \boldsymbol{E} + \boldsymbol{k}^2 \boldsymbol{E} = 0 \tag{3.12}$$

3.2 Light and matter

Explaining physical phenomena often comes down to choice of explanatory model. What is unreasonably simplistic in one context is perfectly suitable in another. For the purposes of the following reasoning, matter can be modeled as a collection of discrete charges living in a world of classical physics. In a material subjected to an electromagnetic wave, its containing free charges will be driven into oscillatory motion. As seen in the Maxwell equations this itself, moving charges, generates further oscillating electromagnetic fields, otherwise known as secondary radiation or *scattered* light[54]. A number of phenomena usually not thought of as scattering can be understood through this model. As atoms are subjected to an electric field, the negatively charged electrons and the positively charged nuclei are driven out of positional equilibrium due to the field induced generation of an oppositely directed force[1]. It can be thought of as the electrons being attached to the

[1]Note that it is primarily the electrons that move due to their lower mass.

nuclei with a spring and thus acting as driven damped oscillators. Matter subjected to light, oscillating electromagnetic fields, thus become a collection of oscillating charges which themselves generates oscillating fields. In other words, they will radiate electromagnetic energy; scatter light. The force a single electron in a material is subjected to is thus the combined effect of the incoming electric field and what is generated from all other electrons. The interactions of these coupled oscillators, making up matter, thus boils down to a rather complicated electromagnetic many-body problem whose solutions describe a wide range of phenomena such as specular and diffuse reflection, diffraction by slits and gratings and refraction between different media[54].

This model further provides a framework for the following discussion of three concepts of particular interest for this work: refractive index, dielectric media and Rayleigh-Gans-Debye (RGD) scattering theory[54].

3.3 Refractive index and dielectric media

At this point the time is come to introduce one of the central concepts of this thesis, the *refractive index*. This material property is defined as the ratio between the in vacuo speed of light and its medium phase velocity. This in media phase velocity decrease can be derived as a direct result of the above discussed electromagnetic model. The combination of an incoming field and the scattered light it induces in a material is manifested as an apparent decrease in phase velocity[54]. Besides this, there are a number of intricacies to this parameter upon which many methods and results rely:

Building upon section 3.1, an interesting result is obtained by taking the cross product of $\boldsymbol{k}$ with equation 3.9.

$$\boldsymbol{k} \times (\boldsymbol{k} \times \boldsymbol{E}_0) = \omega \boldsymbol{k} \times \boldsymbol{B}_0 = -\omega^2 \varepsilon \mu \boldsymbol{E}_0 \tag{3.13}$$

This, through the previously introduced useful vector identity, gives:

$$\boldsymbol{k} \cdot \boldsymbol{k} = \omega^2 \varepsilon \mu \tag{3.14}$$

and thus an expression for $\boldsymbol{k}$:

$$|\boldsymbol{k}| = \omega \sqrt{\varepsilon \mu} = \frac{\omega}{c} \sqrt{\varepsilon_r \mu_r} = \frac{\omega}{c} N \tag{3.15}$$

With N being the complex refractive index of the medium in which the wave is propagating.

$$N = \sqrt{\varepsilon_r \mu_r} = \sqrt{\frac{\varepsilon \mu}{\varepsilon_0 \mu_0}} = n + i\kappa \tag{3.16}$$

where the real part $\Re(N) = n$ is what is commonly referred to as the refractive index whereas $\Im(N) = \kappa$ is a parameter governing attenuation. The latter is evident when considering the $-i\boldsymbol{k}\cdot\boldsymbol{x}$-term in the field expression exponents (e.g. equations 3.7 and 3.8), where the imaginary part of $\boldsymbol{k}$ produces a negative exponent and thus spatially decaying fields.

Many materials, including those of interest in this thesis, are practically non-magnetic and consequently have a relative permeability μ_r close to unity. In these cases the refractive index can be approximated as $\sqrt{\varepsilon_r}$. One convenient route to comprehension of N is thus to understand the ε_r-parameter, the relative permittivity of a material.

The reader is hence encouraged to recall the features of the relative permittivity as it thus translates to N and is of high importance in the following context. In the case of a dielectric material, by definition where $\boldsymbol{k'} >> \boldsymbol{k''}$, the complex relative permittivity, $\varepsilon_r(\lambda) = \varepsilon'(\lambda) - i\varepsilon''(\lambda)$ is a wavelength dependent quantity whose real part is a measure of the material electric polarizability, the extent to which the material is polarized upon exposure to an electric field, while its imaginary part describes the attenuation of electric fields passing through the material, the latter often manifested as *absorption* of light. ε' thus describes the how much the material electrons are displaced from equilibrium to counteract the applied field; it is the spring constant of our recently introduced analogy of electronic springs. A higher refractive index does consequently, besides the decreased light phase velocity, denote weaker internal electric fields.

In the case of dielectric solutions, the refractive index relates to the convenient relation referred to as the *refractive index increment*, $\partial n/\partial c$, which highlights its dependence on solute mass concentration. The fact that the refractive index increment is near constant in a wide concentration range for biological compounds, such as proteins and phospholipids, has promoted thorough investigation and tabulation of its material specific values[55]. This can accordingly be utilized for protein film surface mass concentration, Γ through the, so called, de Feijter's formula:

$$\Gamma = \frac{\Delta d_p(n_p - n_m)}{\partial n/\partial c} \tag{3.17}$$

where n_p and n_m is the refractive indices of protein film and bulk solution, respectively, and d_p the protein film thickness[56].

It has been shown that the refractive index increment of protein can, with great accuracy, be predicted based on its constituent amino acid composition[55]. The expression uses the mass weighted average values (referred to with subscript i) of two known amino acid specific parameters, refraction per gram R_a and specific volume $\bar{\nu}_a$ (i.e inverse density), expressed as follows[55]:

$$R_i = \frac{\sum_a R_a M_a}{\sum_a M_a} \tag{3.18}$$

$$\bar{\nu}_i = \frac{\sum_a \bar{\nu}_a M_a}{\sum_a M_a} \tag{3.19}$$

where M_a is the amino acid molar mass.

These parameters relate to the protein refractive index as

$$n_p = \sqrt{\frac{2R_i + \bar{\nu}_i}{\bar{\nu}_i - R_i}} \tag{3.20}$$

which in turn relates to the refractive index increment as

$$\partial n/\partial c = \frac{3}{2}\bar{\nu}_i n_0 \frac{n_p^2 - n_0^2}{n_p^2 + 2n_0^2} \tag{3.21}$$

with n_0 being the refractive index of the solution[55].

3.4 Scattering of light by lipid vesicles

Scattering of light, the excitation of charge oscillations and consequent elastic[2] reemission of electromagnetic radiation due to refractive index contrasts, is rigorously described through the Maxwell equations[54]. However, a thorough phenomenological discussion of scattering using this foundation directly risks distracting from the special cases of interest in this work, namely scattering of light of vesicles in the $\sim 100\,\mathrm{nm}$ diameter range as discussed in Paper I. More specifically, the interest of this thesis work lies in the change in scattering intensity of a vesicle upon surface adhesion of a protein layer.

An appropriate starting point for the modeling of this special case is the scattering of an infinitesimally small oscillating dipole, the light scattering of which can be expressed as[57]:

$$\boldsymbol{I_s}(\alpha) = \frac{\pi^2 \alpha^2 |\boldsymbol{E}^2| c}{2\varepsilon\lambda^4} \left(\frac{\sin\theta}{r'}\right)^2 \hat{\boldsymbol{r}} \tag{3.22}$$

where c is the in media speed of light, λ the incident light wavelength, $\boldsymbol{E}$ the applied electric field, α the polarizability, ε the permittivity, $\hat{\boldsymbol{r}}$ a unit vector and r' and θ being spherical coordinates. The $\sin\theta$-factor describes the apparent dipole moment dependence on the angle of observation. Depending on observational setup, it is necessary to integrate over an appropriate angle range to find correct values.

The assumption of an infinitesimally small scattering dipole as a model does, together with the assumption of a refractive index close to 1, produce the premises for the Rayleigh

[2] I.e. where the kinetic energy is conserved.

scattering model[52], which was developed by its eponym in the 1800s[58]. Particles in this size and refractive index range (basically, non-metallic particles with a size $\sim 1/10$ the light wavelength) can be considered small enough to have a negligible internal phase shift.

In this case, the polarizability, α_v, for a vesicle can be modeled as a hollow sphere (consisting of a lipid bilayer)[54]:

$$\alpha_v = 4\pi r^3 \frac{(2\varepsilon_l + \varepsilon_m)(\varepsilon_l - \varepsilon_m)(1-\varphi)}{(\varepsilon_l + 2\varepsilon_m)(\varepsilon_l + \varepsilon_m) - 2(\varepsilon_l - \varepsilon_m)^2\varphi} \tag{3.23}$$

where ε_l and ε_m is the lipid and medium permittivities, r the vesicle radius and $\varphi = (r-\Delta_l)^3/r^3$ the fraction of the total vesicle volume not occupied by the bilayer (with Δ_l being the bilayer thickness). Since the bilayer is thin compared with the vesicle, $\Delta_l << r$, φ can be approximated as $1-\varphi = 3\Delta_l/r$ and $\varphi = 1$ in the numerator and denominator, respectively. This yields:

$$\alpha_v = \frac{4\pi r^2 \Delta_l (2\varepsilon_l + \varepsilon_m)(\varepsilon_l - \varepsilon_m)}{3\varepsilon_l \varepsilon_m} \tag{3.24}$$

A vesicle with attached proteins can be viewed as a two-shell system, where to the lipid bilayer, an external shell of thickness Δ_p and permittivity ε_p is added. Still under the assumption of small shell thicknesses in comparison with the vesicle radius r, the two shells can be replaced by one effective shell with the thickness

$$\Delta_{lp} = \Delta_l + \Delta_p \tag{3.25}$$

and permittivity

$$\varepsilon_{lp} = \frac{\varepsilon_l \Delta_l + \varepsilon_p \Delta_p}{\Delta_l + \Delta_p} \tag{3.26}$$

Consequently, the vesicle protein complex has a polarizability of

$$\alpha_{v,p} = \frac{4\pi r^2 \Delta_{lp} (2\varepsilon_{lp} + \varepsilon_m)(\varepsilon_{lp} - \varepsilon_m)}{3\varepsilon_{lp}\varepsilon_m} \tag{3.27}$$

The ratio of scattering intensity increase to initial scattering intensity, i.e scattering due to the adhered protein layer to the prior scattering from the vesicle can be expressed

$$\frac{\Delta I_s}{I_0} = \frac{I_s(\alpha_{v,p}) - I_s(\alpha_v)}{I_s(\alpha_v)} = \frac{\alpha_{v,p}^2 - \alpha_v^2}{\alpha_v^2} \tag{3.28}$$

Measuring the scattering intensity ratio thus provides, through equations 3.24, 3.27 and 3.28, a relation between the thicknesses and permittivities of the protein layer and lipid bilayer which to the first order approximation is size independent.

When the particle size approaches that of the wavelength of the excitation light, two main phenomena of interest to us arise: i) interference of light scattered from different parts of the particles and ii) potential inhomogeneous illumination intensity. The latter is relevant here due to the use of an exponentially decaying evanescent illumination field in the waveguide microscopy method (see the following section) while the former plays a minor role in the present case (of particles $\sim 100\,\text{nm}$ in diameter) but becomes more significant when extending the data interpretation to larger particles. This is the subject of the, so called, Rayleigh-Gans-Debye approximation which combines the Rayleigh approximation with internal phase retardation and considers solely first order scattering[54].

These effects can be summarized as introducing a correction factor f_s, taking these phenomena into account, where $f_s = 1$ recovers the Rayleigh approximation.

$$I_s = I_s^0 f_s \tag{3.29}$$

Thorough derivation of f_s for lipid vesicles in the size range of interest ($\sim 100\,\text{nm}$ in diameter) can be found in the supporting information of the referenced articles[59, 60]. The main idea is to use a volume integral taking phase shift and spatial illumination decay into account. The results can be summarized as:

$$f_s = \chi^2 \approx \chi_{ev}^2 \chi_{ph}^2 \tag{3.30}$$

with

$$\chi_{ev} = (\delta/r)[1 - \exp(-r/\delta)]. \tag{3.31}$$

and

$$\chi_{ph} = \frac{\sin[2k\sin(\theta/2)r]}{2k\sin(\theta/2)r} \tag{3.32}$$

Here, δ is the evanescent field decay length (see the following section). Using this correction factor, the scattering intensity of small particles can be adequately described, provided that the particles size and relative refractive index compared to the surrounding medium are not too large

3.5 Waveguide theory

A phenomenon of immense use in biophysical research is that of a, so called, *evanescent field* for illumination of near-surface nanoscopic objects. When a propagating electromagnetic wave encounters an interface with a discrete decrease in refractive index, e.g. light passing from glass to water or water to air; *total internal reflection*, the reflection of all incoming

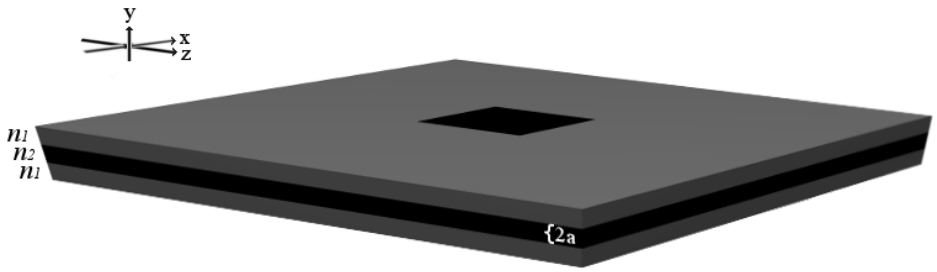

Figure 3.1: Illustration of a waveguide chip as used in this work. A (black) core layer of refractive index n_2 is enveloped by the (grey) cladding layers of refractive index n_1. Confinement of light in the core is possible if $n_2 > n_1$. Note that this image is not to scale and that the core and cladding layers having a thickness of approximately 0.4 µm and 3 µm, respectively; deposited on a ~ 500 µm silicon wafer. The core thickness is here defined as $2a$, with the y-coordinate zero being placed in its center.

energy, occurs above a certain critical incident angle[52]. Total reflection of light is however not a discrete phenomenon but is a consequence of the incident light inducing charge oscillations which under these conditions interact to have destructive interference in the forward direction. While this indeed results in total reflection in the far-field, the oscillating charges actually produce a local near-field, a propagating field along the interface which decays exponentially with distance from the interface, the evanescent field. This thin field of light, which in common practical microscopy setups has a penetration depth of a few hundred nanometers, is conveniently utilized for illumination of surface bound entities e.g. in total internal reflection fluorescence microscopy (TIRFM)[61]. One of the main motivations for utilizing this type of illumination scheme is that by solely illuminating near-surface entities, signals stemming from the bulk are minimized.

Another technological approach to generate and use an evanescent field is that of adjacent slabs of different refractive index, a planar waveguide. Figure 3.1 shows an illustration of the relevant situation, highlighting the *waveguide core* (of refractive index n_2) sandwiched in-between layers of lower refractive index material (n_1) referred to as the *cladding* layers. Light propagating in the x-direction in the core in this situation can be approximated as a plane wave according to equation 3.7 (assuming a thin waveguide core, and thus solely a single mode), but noting that the materials extending semi-infinitely in the z-direction allows for the expression of the time-independent electric field to be expressed independently of this dimension, i.e.:

$$\boldsymbol{E}(\boldsymbol{r}) = \boldsymbol{E}(y)e^{-i\beta x} \tag{3.33}$$

where β is the wavenumber of light traveling in the waveguide in the x-direction.

This expression in combination with equation (3.12) gives:

$$\frac{\partial^2 \boldsymbol{E}}{\partial y^2} + (k^2 - \beta^2)\boldsymbol{E} = 0 \tag{3.34}$$

With $n_2 > n_1$, the $(k^2-\beta^2)$-factor will be positive for the core and negative for the cladding. This results in equation (3.34) having the following solutions:

$$E = \begin{cases} A\cos(a\sqrt{k^2 n_1^2 - \beta^2} - \varphi)e^{-\sqrt{\beta^2 - k^2 n_2^2}(y-a)} & y > a \\ A\cos(x\sqrt{k^2 n_1^2 - \beta^2} - \varphi) & -a < y < a \\ A\cos(a\sqrt{k^2 n_1^2 - \beta^2} + \varphi)e^{\sqrt{\beta^2 - k^2 n_2^2}(y+a)} & y < -a \end{cases} \tag{3.35}$$

where a is half the thickness of the core layer; A is a constant that can be derived from the boundary condition of the electric field and φ a phase term[62].

Consideration of these equations reveal a propagating field in the waveguide core and, the exponentially decaying evanescent fields in the cladding layers. A convenient quantitative characterization of these types of decaying fields is that of a decay length or penetration depth, δ, defined at the distance where the field intensity has decreased with a factor of $1/e$:

$$\delta = \frac{1}{\sqrt{\beta^2 - k_{\text{cladding}}^2}} \tag{3.36}$$

Paper I uses a waveguide microscopy platform for investigation of protein binding to vesicles. It consists of a silica core ($n_2 = 1.42$) enveloped in cladding layer of the fluorinated polymer material CYTOP ($n_1 = 1.34$). This results in a decay length of $\sim 100\,\text{nm}$. Details of the experimental setup is found in section 4.1.

3.6 Fluorescence

The use of the fluorescence phenomenon in its many implementations is one of the central concepts in the investigation of biological structures and processes[63]. The waveguide microscopy method utilized in paper I benefits from the possibility of combining its scattering microscopy capabilities with that of the more traditional fluorescence microscopy-based investigations.

The method is based on the use of *fluorescent labels*, entities which can bind to analytes of interest which upon absorption of light in a certain spectral range, emit photons of a (usually) increased wavelength[63]. This allows, as in the case of the waveguide microscopy setup described in section 4.1, for the decoupling of the incident and emitted light and thus the selective visualization of labeled objects. The concept is usually explained through the

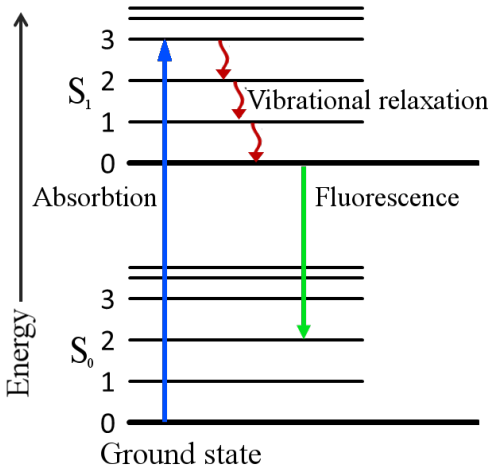

Figure 3.2: The concept of fluorescence illustrated through a Jablonski diagram. An example of the fluorescence process is shown, where excitation of an electron from its ground state S_0 to its first excited singlet state, S_1, through the absorption of a photon and subsequent non-radiative vibrational relaxation (phononic loss of energy) leads to the emission of a photon of increased wavelength (i.e. of less energy). The difference in wavelength between incident and emitted light can be utilized through optical filtering for highly sensitive observation of fluorescing objects.

use of a Jablonski diagram, see figure 3.2 where electronic state transitions in a fluorescent molecule are shown and photon absorption and emission are highlighted.

It is also worth mentioning that the highly reactive nature of fluorophores in their excited state results in the phenomenon of *photobleaching*, where a fluorophore has a certain probability of suffering a photochemical alteration that permanently makes it non-fluorescent. This is often manifested as a fluorescence signal decrease over time, an effect which puts temporal limits on experiments utilization of fluorophores[63].

Since fluorescence emission is in practice fully incoherent, the fluorescence intensity of a labeled object scales with the number of fluorophores (disregarding quenching effects, fluorescence decrease due to a number of phenomena, many which relate to interactions with other nearby entities[63]). This is an important point when comparing a signal based on fluorescence emission with a light scattering signal of the same sample. The scattering signal instead scales with the square of the polarizability (see equations 3.28, 3.23 and results in paper I).

4

Experimental methods

"There is a crack in everything,
that's how the light gets in."

— Leonard Cohen

Practical investigation, understanding and utilization of physical phenomena require, in most cases, experimental measurement in order to acquire necessary information and more often than not, quantitative information is desired. This work focuses on the use of a number of methods and their combination, to investigate the properties and behavior of biological nanoscopic objects. A distinction to keep in mind is that of measurements providing single particle resolved information, such as waveguide scattering microscopy, and that of ensemble average methods, such as SPR and QCM-D, whose signals exclusively originates from multiple particles. This section will provide information on the principles of the main experimental methods utilized in this work.

4.1 Waveguide microscopy

The main method in use for the characterization of individual vesicles utilized here builds on the use of evanescent field illumination through waveguide microscopy, as theoretically outlined in section 3.5. The use of evanescence for this purpose in its currently most popular implementation, total internal reflection fluorescence microscopy, was pioneered by Axelrod in the 1990s[64]. Waveguide microscopy shares many similarities with this method in terms of the use of the rapidly decaying evanescent field for sample illumination. The basic structure of the waveguide chip used consists of a silicon substrate on which a lower cladding, core and upper cladding layer have been sequentially deposited. A single chip (see figure 4.1) consists of a $1 \times 1\,\mathrm{cm}^2$ square of this assembly with a $2 \times 2\,\mathrm{mm}^2$ well etched through the top cladding layer, reaching the waveguide core and thus an excited evanescent field therein. The field is generated through laser illumination through an optical fiber coupled to the waveguide core layer from a chip facet. This illumination setup features an orthogonal relation between the illumination and observation direction, i.e. illumination

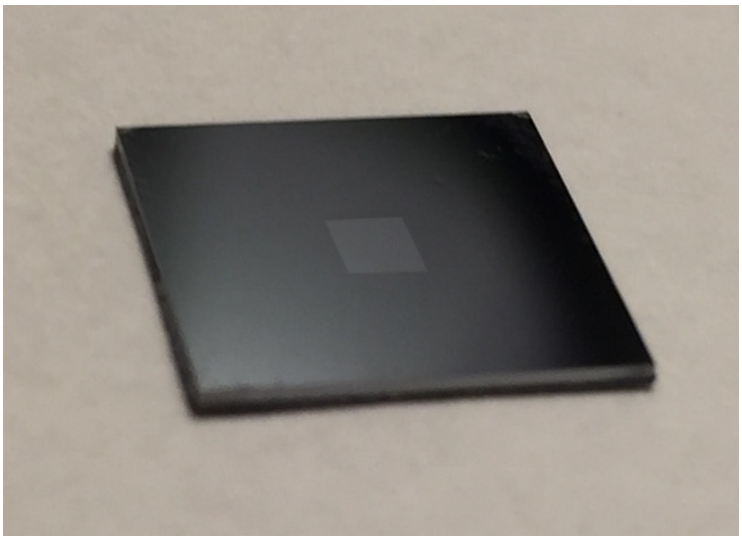

Figure 4.1: Picture of a waveguide chip used in this work. The chip has an area of $1 \times 1\,\mathrm{cm}^2$

from the side and observation from above. This makes the method a *dark field microscopy* method[52], in contrast with conventional TIRFM.

In order to minimize stray light scattering, which as discussed in section 3.2 is a consequence of refractive index contrasts, the cladding consists of CYTOP, a fluorinated polymer material which has the convenient property of a refractive index of 1.34[65] (i.e n_1 in figure 3.1 and equation 3.35), thus closely matching that of water. The cladding envelops a core of silica, in the form of spin-on-glass, with a refractive index of 1.42 (i.e n_2).

A waveguide scattering measurement setup, as implemented in paper I, is shown in figure 4.2. A water immersion objective is connected to a drop of buffer placed in the waveguide well, enabling the observation of objects emitting light due to the generated evanescent field on the well bottom. This entails light emitted due to fluorescence excitation and emission, in a manner analogue to that of TIRF microscopy, but also scattered light due to refractive index contrast of an object and the surrounding medium. The penetration depth of the waveguide system, which defines its sensing range extending from the core, is determined by the refractive indices and thicknesses of the core and cladding layers and can be tuned from below 100 nm to well above a micron[66], while regular TIRF usually exhibits 100-200 nm values. The implementation used in this thesis shows a penetration depth of approximately 100 nm.

The many intricacies of manufacturing this waveguide system are discussed in several publications, to which the interested reader is referred[59, 67].

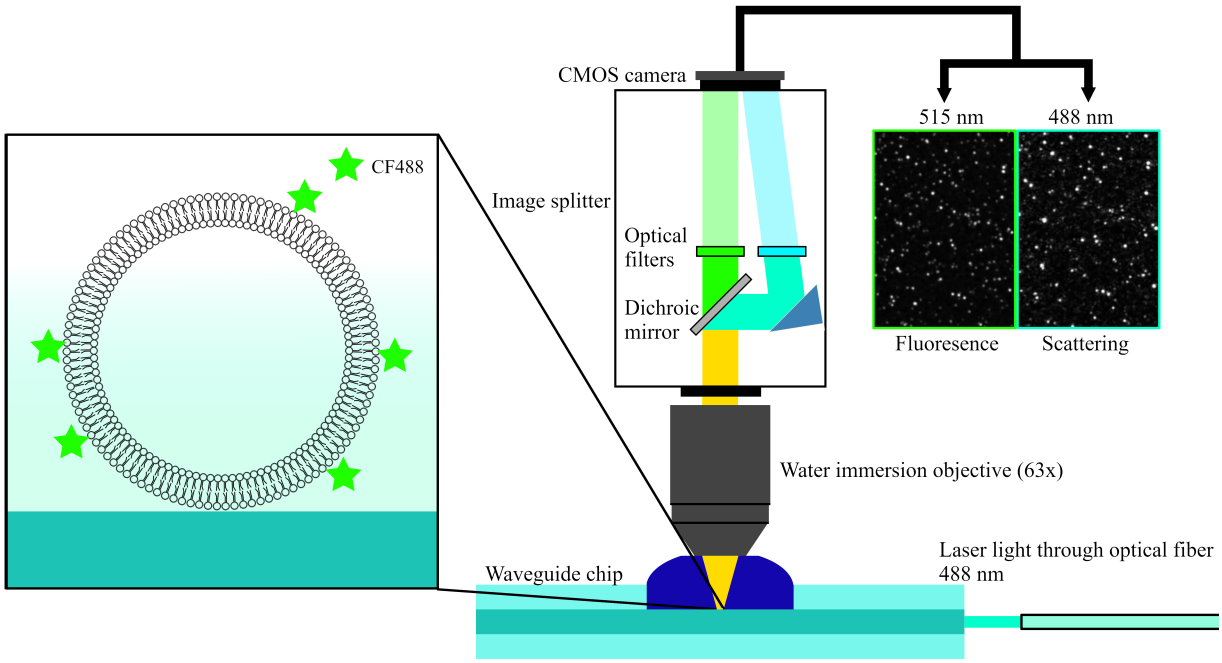

Figure 4.2: Illustration of the basic principle of a waveguide evanescent light measurement. Laser light of a certain chosen wavelength, here 488 nm, is coupled from an optical fiber to the waveguide core in which a propagating field, and outside of which an exponentially decaying evanescent field, is generated. A drop of solution which constitutes the experimental environment and contains analytes of interest has been placed in the waveguide well which provides access to the evanescent field on the core surface. A vesicle partially consisting of fluorescently labeled lipids (CF488 labels) is found inside the evanescent field, which causes it to scatter light of 488 nm and fluoresce at approximately 515 nm. This light passes through an objective immersed in the solution droplet and subsequently through an image splitter which separates the two signals which are subsequently projected onto a CMOS camera.

4.2 Surface plasmon resonance sensing

The defining property of a metal is, I believe most students of physics would explain, the feature of cations in a background of commonly contributed delocalized electrons, or expressed in analogical language, the *electron sea*. These free electrons, or plasma, act as a main mediator of many defining properties of this material class, for example its electrical conductivity. Extending the marine analogy further it is possible to excite waves in the electron sea, so called surface *plasma oscillations* or *surface plasmons*, electron density oscillations which, although the charges are highly confined to the metal surface, generate fields extending into the local environment[68]. The generation of surface plasmons in a metal depends on a set of conditions which, if properly fulfilled, causes an energetic maximum; this occurs at the, so called, resonance conditions. Keeping in mind the existence

Figure 4.3: Medieval application of localized surface plasmon resonance. Light in certain wavelength intervals is absorbed and scattered by metal nanoparticles in the glass, producing colorful results. Notre-Dame de Paris.

of other types of plasmonic excitations, such as bulk and wire plasmons[69], the following discussion is restricted to the case of surface plasmon resonance (SPR).

Utilized since at least around 300 AD[70] for fabricating stained glass[1] (see figure 4.3), properly understood in the late 1960s[71, 72] and applied for biosensing purposes since the 1980s[73], the plasmon resonance phenomenon is an intriguing and colorful concept. The principle behind the main bioanalytical technology utilizing this phenomenon, *surface* plasmon resonance builds on the possibility to excite propagating electron density oscillations at a metal-dielectric interface. The field generated from surface plasmons exhibits exponential decay into the local environment and SPR biosensors thus produces a situation similar to the above discussed evanescent field waveguide microscopy method, where analytes are placed in an exponentially decaying field above a surface.

As electrons in a metal surface are driven out of positional equilibrium due to plasmonic excitation, they are subjected to a retrogradely directed force stemming from the mutually repulsive interactions of the equally charged electrons. This is the driving mechanism of the resulting electronic oscillatory behavior, i.e. the plasmons. As theoretically discussed in section 3.3, the refractive index of a medium relates to its extent of electromagnetic field attenuation. An increase in refractive index in the region above a metal surface, for example by the replacement of water with an optically more dense material such as a biomolecular entity, will thus reduce the magnitude of the restoring force felt by the electrons which thus reduces the plasma oscillation frequency. This is the basic principle behind SPR based biosensing. Refractive index variations due to the presence and behavior of biological analytes close to a surface affects the plasmon resonance frequency which, if gauged, thus provides information interpretable in terms of analyte presence, mass, structure and dynamics.

[1]Note that this specific application relates to the *localized* surface plasmon resonance phenomenon, which is further discussed in section 4.2.1.

From a technological perspective it is convenient to excite plasmons through the use of light, in particular laser illumination. Generation of SPR at a metal-dielectric interface (in biosensing applications commonly gold-water) through these means is, however, nontrivial due to the need of simultaneous matching of both energy and momentum between the light and surface plasmon[68]. Of the two existing main methods for adding the required extra momentum, grating based and prism based, the latter, called the Kretschmann configuration is more common as it allows for more technologically elegant solutions and will be in focus henceforth. In this context, the required momentum matching can be expressed as matching the metal surface parallel components of the laser illumination wavevector incident through the glass prism, $k_{i,x}$, with the surface plasmon wavevector, $k_{sp,x}$.

Under the, for our purposes, reasonable assumptions of typical material properties, metal similar to an electron plasma and non-lossy dielectric (i.e $-\Re(\varepsilon_d) > \varepsilon_m$, $-\Re(\varepsilon_d) >> \Im(\varepsilon_d)$, $\Im(\varepsilon_m) \approx 0$), allows expressing the real part of the propagating plasmon wavevector as:

$$\Re(k_{sp,x}) = \frac{\omega}{c}\sqrt{\frac{\Re(\varepsilon_d)\varepsilon_m}{\Re(\varepsilon_d) + \varepsilon_m}} \tag{4.1}$$

where ω is the angular frequency, c the speed of light, ε_d the permittivity of the dielectric, ε_m the permittivity of the metal[74].

$k_{i,x}$ of illumination incident through the prism with an angle θ can be expressed as[68]:

$$k_{i,x} = \frac{\omega}{c}\sqrt{\varepsilon_g}\sin(\theta) \tag{4.2}$$

In the experimental setup in use in this work, the angle of illumination θ is continuously varied across a chosen interval as the subsequent reflection is observed. As $k_{i,x}$ and $k_{sp,x}$ coincides and surface plasmon resonance excitement occurs, this is manifested as a reflection intensity minimum. The angle θ at which this occurs can be tracked over time, for example as material adheres to the surface, and constitutes a major signal of an SPR measurement (see figure 4.4). This minimum angle is henceforth referred to as the SPR response, R.

The above reasoning on how the SPR response relates to environmental refractive index variations is evident from equation 4.1 which shows that the plasmon wavevector is a function of the dielectric permittivity, ε_d, thus its refractive index ($n_d = \sqrt{\varepsilon_d}$).

The instrument in use in this work, the SPR Navi 220A instrument (BioNavis) provides the simultaneous use of two SPR excitation wavelength, in this case 670 nm and 785 nm, allowing for more extensive data analysis. The sensors in use are gold surfaces on glass substrates coated with a thin (10-20 nm) SiO_2 layer in order to allow desired surface chemistry.

The quantitative aims of this work require the interpretation of the SPR response in terms of relevant analyte parameters, i.e. mass and dimensions of entities adhered to the sensor

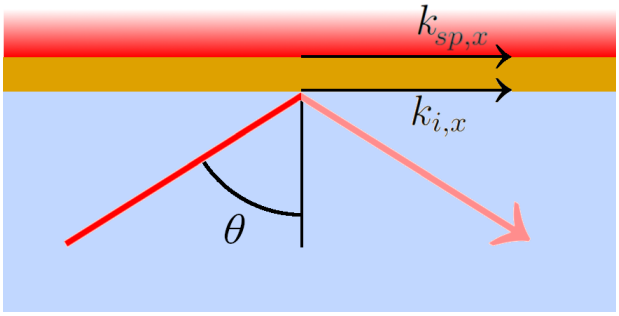

Figure 4.4: The working principles of the surface plasmon resonance sensing method utilized in this work. When the metal surface parallel component of the laser illumination wavevector incident through the glass prism, $k_{i,x}$, coincides with the surface plasmon wavevector, $k_{sp,x}$, SPR excitation occurs. This happens at a certain laser illumination angle θ which is determined by continuously varying the illumination angle and observing the reflection intensity minimum. θ, also referred to as the SPR response R, additionally depends on the refractive index above the sensor surface and can thus be used as a gauge for this parameter. How this response is manifested during the addition of samples of different dimensions and refractive index can be seen in figure 5.5.

surface. The key bridge between refractive index and mass concentration Γ, as discussed in section 3.3, is the de Feijter's formula:

$$\Gamma = \frac{d_f(n_f - n_m)}{\partial n/\partial c} \tag{4.3}$$

with n_f and n_m being the refractive indices of an adhered film and bulk solution, respectively, and d_f the film thickness[56]. Interpretation of the SPR response, R, in terms of refractive index thus provides a route to mass determination. The most straightforward way for this is to assume a linear relationship between R and Δn, an assumption which holds for a small Δn[75], i.e:

$$R_\lambda = S_\lambda(n_{f,eff} - n_b)_\lambda \tag{4.4}$$

where the subscript λ indicates the parameter wavelength dependence, $n_{f,eff}$ is the effective refractive index of an adhered film, taking the exponentially decaying nature of the plasmon field into account, and S is the SPR instrument sensitivity, a factor describing the signal response per refractive index unit which in practice is determined through calibration measurements with solutions of known refractive index (in this work H_2O- or D_2O-based buffer or glycerol).

Expression of the effective refractive index of an adhered film of refractive index n_f and thickness d_f[75] enables the following relation:

$$R_\lambda = S_\lambda(n_f - n_m)_\lambda \phi(d_f,\delta_\lambda) \tag{4.5}$$

With ϕ being a dimensionless parameter accounting for the plasmon field decay:

$$\phi(d_f,\delta) = 1 - e^{-d_f/\delta} \tag{4.6}$$

Combining this expression with equation 4.3 provides an expression for the bound mass concentration:

$$\Delta\Gamma = \frac{R_\lambda d_f}{S_\lambda(\partial n_\lambda/\partial c)\phi(d_f,\delta_\lambda)} \tag{4.7}$$

As is evident above, determination Γ requires a value for d_f, value which can be obtained from parallel measurements through other instrumentation or circumvented through approximation[76].

A convenient alternative to this approach is the utilization of a second SPR illumination wavelength with the purpose reducing the number of required approximations by determining d_f directly from the measured response ratio[77]. This dual-wavelength SPR method exploits the fact that surface plasmons induced by different illumination wavelengths differ in field decay length and thus senses refractive index variations at different depths. As a volume of bulk solution in the vicinity of the sensor surface is replaced by sample, the resulting effective refractive index change of the total sensing volume will differ between wavelengths. This allows for the analysis of sample dimensions/geometry in addition to the conventional mass quantification. Through consideration of the response ratio between the wavelengths, the use of dual wavelengths further eliminates potential inaccuracies due to assumptions on absolute component refractive index values. Since S_λ, the component refractive index increments and δ_λ and their wavelength dependencies are known, the simultaneous dual response acquisition, in this case at 670 nm and 785 nm, and consideration of their ratio enables calculating the adsorbed film thickness d_f using the following expression:

$$\frac{R_{670}}{R_{785}} = \frac{S_{670}(\partial n/\partial c)_{670}\phi(d_f,\delta_{670})}{S_{785}(\partial n/\partial c)_{785}\phi(d_f,\delta_{785})} \tag{4.8}$$

where $(\partial n/\partial c)_{670}/(\partial n/\partial c)_{785} \approx 1.02$[78].

This expression is illustrated for a homogeneous film in figure 4.5a), where the response ratio is plotted as a function of the film thickness d_f. A measured R_{670}/R_{785}-value can accordingly be interpreted as a film thickness.

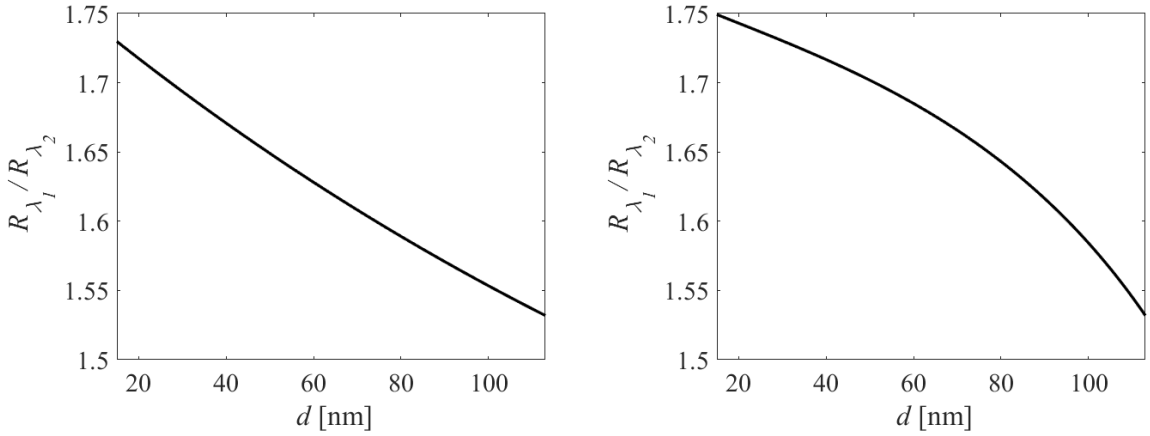

Figure 4.5: The response ratio for $\lambda_1 = 670$ nm and $\lambda_2 = 785$ nm as a function of film thickness d. (a) shows the function for a nondeformed vesicle which has a laterally symmetric mass distribution and thus a ϕ according to equation 4.6. (b) shows the function for a vesicle deformed according to figure 4.6 and thus with a ϕ according to equation 4.9, calculated with a radius $r = 52.5$ nm prior to deformation.

The expressions above, which assumes thin films adhered to the SPR sensor surface, has mathematically been shown to be equal when replacing a homogeneous film with vesicles with a radius $r = d_f/2$, under the assumption of negligible vesicle deformation upon interaction with the underlying surface, i.e. mirror symmetric vesicles along an axis perpendicular to the surface[77]. In situations where this assumption is not valid, such as in paper II, an asymmetric distribution of the vesicle material needs to be considered. A model for this, where vesicles are deformed into truncated spheres but with maintained surface area (see reference[77]), can be implemented by expressing ϕ as:

$$\phi(r,\delta) = [a^2 + 2\delta\rho(1 - \exp\{-(\rho + \sqrt{\rho^2 - a^2})/\delta\})]/2r\delta \tag{4.9}$$

with a and ρ being geometric parameters of the truncated sphere as defined in figure 4.6. These parameters are related to the radius r of the vesicle prior to deformation and the thickness d after deformation according to

$$\rho = \frac{4r^2 + d^2}{4d} \tag{4.10}$$

See paper II for a more thorough discussion on this model. This expression thus allows the expansion of the vesicle thickness determination methodology outlined above to include deformed vesicles.

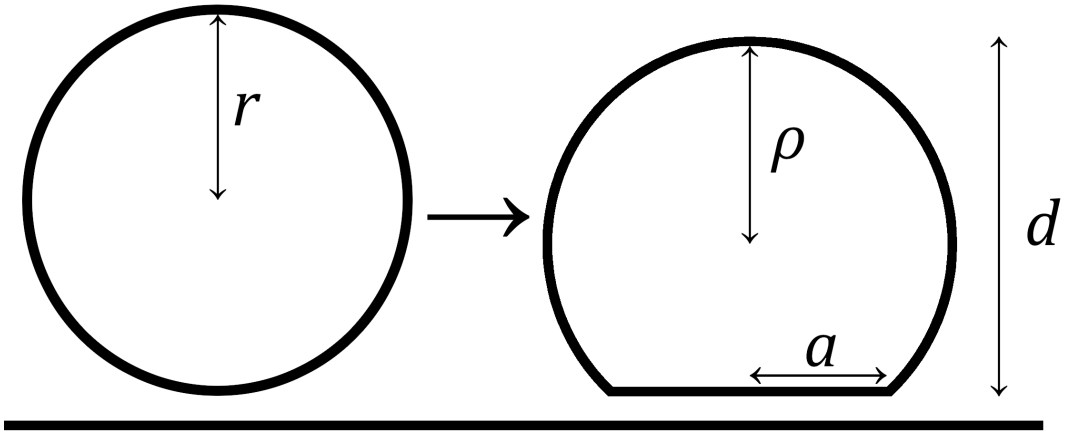

Figure 4.6: Liposome deformation is modeled as a sphere of radius r transitioning to a truncated sphere of radius ρ and footprint radius a while the particle area is preserved. Prior to deformation the liposome lateral dimension, i.e. the thickness as measured using SPR, is simply $2r$, while it after deformation equals d, relating to ρ and a as expressed in equation 4.10.

4.2.1 Localized surface plasmon resonance

Besides SPR, there has been efforts in implementing and commercializing an alternative plasmon based biosensing technology[79], based on the related phenomenon of *localized* surface plasmon resonance (LSPR). This method utilizes excitation of plasmonic resonance in metal nanoparticles in contrast with the two-dimensional metal surfaces in use in conventional SPR biosensing. This difference has, from a user perspective, two major consequences: Easier plasmon excitation and smaller decay length.

Due to confinement in a nanoscopic particle, the localized plasmons are non-propagating and thus carry no momentum. This eliminates the need of the momentum matching discussed in the previous section and leads to substantially easier excitation of plasmons. In fact, metal nanoparticles in a certain size range will permit plasmonic excitation solely from illumination. A fact evident when observing stained glass, whose color often stems from plasmonic nanoparticles scattering and absorbing light in parts of the visible spectrum due to coincidence with their plasmon resonance (see figure 4.3). A LSPR biosensing measurement is thus commonly implemented through spectroscopy. Plasmonic nanoparticles are illuminated with white light during simultaneous spectroscopic analyzation as the environmental refractive index varies due to biomolecular events occurring within the plasmon sensing depth.

When discussing spectral variations of nanoparticles, it is useful to do so in terms of *light extinction*, σ_{ext}, the wavelength dependent combined effects of the particle light scattering and absorption. In simple terms, how the measured spectrum is changed when introducing the particles between a light source and a detector.

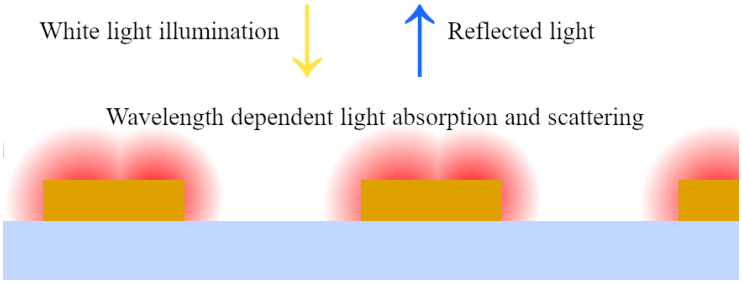

Figure 4.7: The working principles of the localized surface plasmon resonance sensing method utilized in this work. Metal nanoparticles on the sensor surface will, upon white light illumination, exhibit wavelength dependent scattering and absorption of light due to the excitation of LSPR. The wavelengths at which this occurs depends on a range of parameters such as nanoparticle size, shape and material but also on the environmental refractive index. Determination of the wavelength of maximum extinction, i.e. where the most energy is lost to the LSPR, can thus be utilized for refractive index sensing close to the nanoparticles. This can for instance be used for mass concentration determination of biological samples placed in the nanoparticle vicinity.

For particles small with respect to the wavelength of light λ[80]:

$$\sigma_{ext}(\lambda) = \frac{24\pi^2 r^3 n_m^3}{\lambda} \frac{\varepsilon''(\lambda)}{(\varepsilon'(\lambda) + 2n_m^2)^2 + \varepsilon''(\lambda)^2} \tag{4.11}$$

where $\varepsilon(\lambda) = \varepsilon'(\lambda) - i\varepsilon''(\lambda)$ is the complex permittivity and r the nanoparticle radius.

For gold and silver nanoparticles, where $\varepsilon''(\lambda)$ is small, this expression has a maximum at $\varepsilon'(\lambda) = -2n_m^2$, which is the plasmon resonance condition. This peak position is, as in SPR, dependent on the environmental refractive index and can thus be utilized as the measurement response (see figure 4.7).

The second difference between SPR and LSPR to consider is the significantly shorter decay length of the latter, which is measured in tens of nm instead of hundreds[79]. LSPR thus offers the, to SPR, complementary capabilities of probing effects closer to the sensor surface. In paper I this fact is utilized to investigate distribution of bound proteins to surface immobilized vesicles.

To a first approximation, equation 4.7 can be used for mass estimation here as in the case of SPR. However, due to the significantly lower decay length it is essential to take the sample distance from the sensor surface into account and correct the system sensitivity accordingly.

In this work, the Insplorion Acoulyte instrument was utilized for LSPR analysis of protein binding to vesicles. This instrument is an add-on to the QCM-D instrumentation described below. This equipment thus provide simultaneous LSPR and QCM-D signals and offer

possibilities of comparative analysis. The sensors in use consists of regular QCM-D crystal sensors on which either gold or silver nanodisks have been deposited, on top of which a thin silicon nitride coating has been added for enabling desired surface chemistry.

4.3 Quartz crystal microbalance with dissipation monitoring

Upon the 1959 discovery[81] of a linear relationship between the oscillation frequency response of quartz crystals with mass deposited on its surface, technology exploiting this fact, quartz crystal microbalances, were quickly developed and found use, not least, in layer thickness determination in micro- and nanofabrication[82]. The area of application for this measurement method was significantly expanded from measurement in gas and vacuum to also include aqueous environments with the development of facilitating oscillator circuitry in 1982[83]. This opened the door to the realm of bioanalytical applications where QCM-based technology has occupied its place in the field of label-free ensemble averaged investigations of surface adhered biomolecular compounds.

The method builds on the piezoelectric property of quartz, the fact that physical deformation of the material causes accumulation of electric charge through induced dipole moments, and conversely, that an applied electric field induces deformation. The working principles of QCM-D[82] is built upon the latter through the use of, so called, AT-cut crystals, cut with an 35.25° angle with respect to the optical axis, which upon exposure to an alternating electric field exhibits thickness-shear mode oscillations, i.e. propagating acoustic waves perpendicular to the crystal surface. A quartz crystal will have a set of frequencies, f_n where conditions for resonance are fulfilled. This occurs when the crystal thickness, t_q coincides with an odd number, n, of half wavelengths. The resonance frequency is expressed:

$$f_n = \frac{nv_q}{2t_c} = \frac{nv_q}{\lambda}, n \text{ odd} \tag{4.12}$$

where v_q is the speed of sound in quartz and λ is the induced wave wavelength.

As described in the foundational Sauerbrey paper[81], a change in adsorbed mass to the quartz crystal surface, Δm induces a resonance frequency shift according to:

$$\Delta m = -\frac{C\Delta f}{n} \tag{4.13}$$

Where $C = 17.7\,\mathrm{ng/Hz\,cm^2}$ for the 5 MHz crystals in use in this work. This expression builds on assumptions of thin, rigid and uniform adsorbed films.

By measuring the dissipation of energy following crystal oscillation excitation, it is possible to draw conclusions on the viscoelastic properties of an adherent.

The assumptions of Sauerbrey are often not fully valid when considering measurements involving biomaterials, which usually results in a mass underestimation. By considering information on resonance frequency shifts in combination with energy dissipation from multiple overtones viscoelastic modeling allows for more accurate results[84].

Another effect of great importance in the context is that of coupling of environmental water to a sample, leading to a mass overestimation in comparison to the sample dry mass[85].

In this thesis QCM-D is utilized as a complement to the waveguide microscopy and plasmon resonance measurements for confirming the findings on protein binding to lipid vesicles.

5

Summary of results

"The beauty of science is that all the important things are unpredictable. The optimistic view in me is that nature is designed to make the universe as interesting as possible."

— Freeman Dyson

This section summarizes the two articles which this thesis is based on. More details are found in the appended articles themselves. The figures in this section are in grayscale, but can be found in color in their respective article.

5.1 Paper I

With the objective of developing a quick and reliable, label-free and single-particle-sensitive method for quantification of protein adhesion to BNPs with potential use in pertinent biological environments, waveguide scattering microscopy was implemented and used for the investigation of biotin binding proteins interacting with biotinylated lipid vesicles. The interactions between the chosen proteins and biotin are of common use and well-studied and the full system used consists of, in the context of protein film formation, relatively few components[50, 86]. This results in a system of reduced complexity, suited for method development. Besides investigations through waveguide scattering microscopy, which simultaneously provides a fluorescence signal, SPR, LSPR and QCM-D were utilized on the same system for complementary purposes.

5.1.1 The system

An illustration of the biological system studied can be seen in figure 5.1. The purpose of the system is to produce the interaction of interest in this project, surface presenting vesicles to which fluorescently labelled proteins bind. In order to achieve this final experimental step, a sequence of prior steps are taken:

The experimental procedure consists of the sequential addition of entities to the sensor surfaces, each binding to the previous one, either electrostatically, through cholesterol intercalation into a lipid bilayer, or through the biotin-streptavidin interaction. The final step, in which fluorescently labelled protein bind to biotinylated vesicles, is the main interest of the measurements. The steps were as follows:

1. After method specific cleaning procedures (detailed in the method section of the paper), the sensor surface was functionalized with PLL-g-PEG. This is a synthetic copolymer which consists of a backbone of poly(L-lysine), a positively charged polymer which serves the purpose of electrostatically binding to a negatively charged substrate, to which side-chains of poly(ethylene glycol) has been grafted which forms a dense polymer brush structure which sterically hinders most nonspecific interactions and passivates the surface. A fraction of the sidechains are biotinylated. The biotin biomolecule enables specific binding of biotin-binding entities. Varying the fraction of PLL-g-PEG:PLL-g-PEG-biotin makes possible to control the surface concentration of bound material.

2. The subsequent step consisted of adding a highly concentrated solution of streptavidin which bind to all available biotin on the surface and thus enabled the binding of a second biotinylated substance.

3. In order to enable the binding of vesicles, double stranded DNA tethers with one end biotinylated and the other cholesterolated were added to the surface. This produced a surface of cholesterol which could then intercalate into the lipid bilayers of subsequently added vesicles. These 30 base pair tethers are established as means of binding[34].

4. Subjecting this surface to a lipid vesicle solution lead to their surface immobilization. In this study, unilamellar vesicles consisting of 95 mol% 1-palmitoyl-2-oleoyl-glycero-3-phosphocholine (POPC) and 5 mol% 1,2-distearoyl-sn-glycero-3-phosphoethanolamine-N-[biotinyl(polyethylene glycol)-2000] (DSPE-PEG(2000)-biotin of a diameter of approximately 100 nm are used.

5. To the surface bound lipid vesicles, either streptavidin or anti-biotin IgGs labeled with the CF488 fluorophore were added which leads to the formation of a vesicle-adhered protein film. The protein dimensions ($\sim 30\,\mathrm{nm}^2$) are large in comparison with the area per biotin in the vesicles.

5.1.2 Waveguide microscopy

Observation of the temporal change in scattering and fluorescence intensity during the process of protein binding to the vesicles consistently revealed a signal increase, examples of which can be seen in figure 5.2, both for individual vesicles and as averaged over the approximately 1000 vesicles in the field of view.

The scattering signal for each individual vesicle is interpreted as a mass increase due to

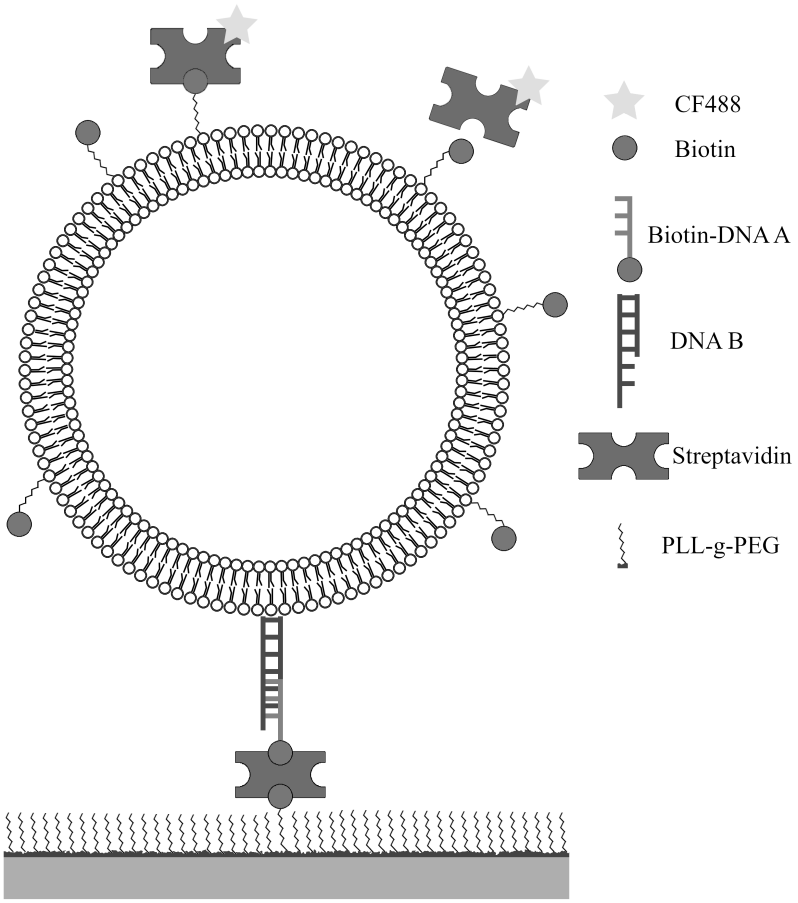

Figure 5.1: Illustration of the system studied. Fluorescently labelled proteins, for example streptavidin, bind to biotinylated vesicles which has been surface immobilized through binding with cholesterolated DNA-tethers, streptavidin and PLL-g-PEG-biotin.

protein binding as discussed in section 3.4. This reveals an adhered protein layer with an average mass concentration of around 200 ng/cm^2 for streptavidin as well as anti-biotin and distributions according to figure 5.3, where the mass concentration increase for individual vesicles, Γ are plotted against the fourth root of vesicle scattering intensity prior to protein binding, $I_{s,v}^{1/4}$, a parameter which scales with the vesicle radius.

In comparison with the other methods, discussed below, the fact that the vesicles are observed at an individual level makes possible the analysis of distributions and sub populations. It also allows for the separation of areas of interest, i.e. the vesicles, from the surrounding surface which in the other cases may contribute signal due to unspecific interactions. This background exclusion is an important advantage in comparison with surface sensitive methods solely relying on ensemble average information.

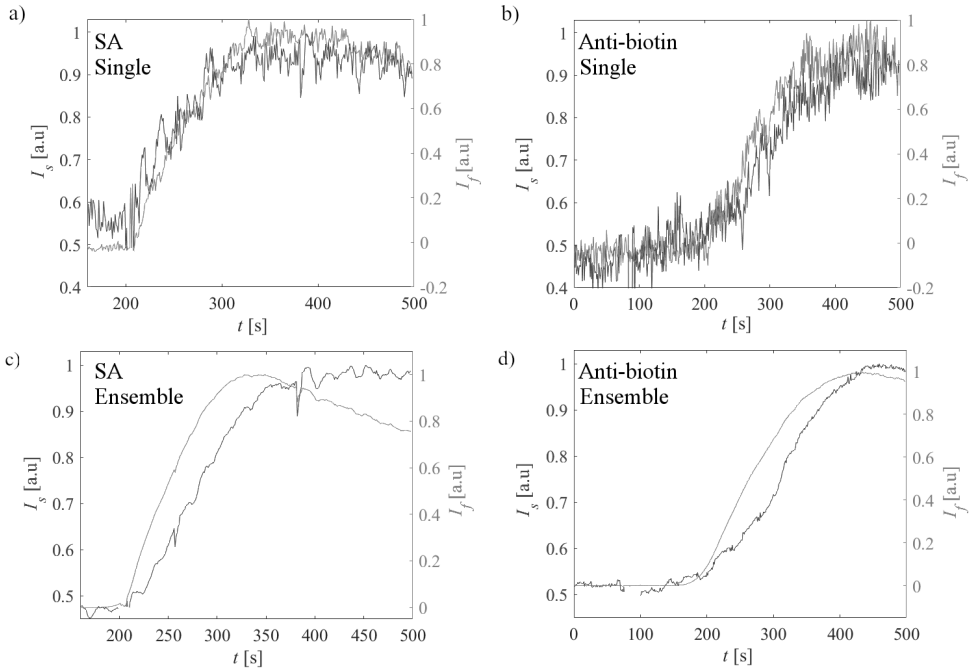

Figure 5.2: Normalized waveguide-microscopy intensities: scattering (blue) and fluorescence (red), as a function of time for biotinylated vesicles upon exposure to protein solutions (CF488-streptavidin or CF488-anti-biotin for the top and bottom row, respectively). a) and b) show the signals for a single representative vesicle while c) and d) show the ensemble average signal for around 1700 vesicles. After signal saturation, the fluorescence intensity decreases over time, due to photobleaching.

5.1.3 SPR, LSPR and QCM-D

Three surface-based ensemble average methods were used in conjunction with the waveguide microscopy, SPR, LSPR and QCM-D. The plasmon based methods required an additional calibration step in which the PBS buffer solution is temporarily exchanged for a D_2O based buffer. The protein mass concentration calculated from the measurement responses was, in the case of streptavidin, 233 ng/cm^2, 275 ng/cm^2 and 630 ng/cm^2 for the three methods, respectively. While the plasmonic methods agrees well with the waveguide microscopy, the QCM-D seemingly overestimates the bound mass as expected due to the included mass of coupled water. The responses upon protein binding to vesicles for all four methods are summarized in figure 5.4.

The SPR and LSPR signals differ in terms of their underlying sensing depth, the prior having significant contributions from the entire vesicle-protein system while the latter sensing mainly the few 10s of nm closest to the substrate. The fact that the responses are very similar suggests that a homogeneous protein distribution and makes it less likely of a binding limited to the top region of the vesicles.

The fact that the QCM-D response is lower when normalized to the vesicle response as

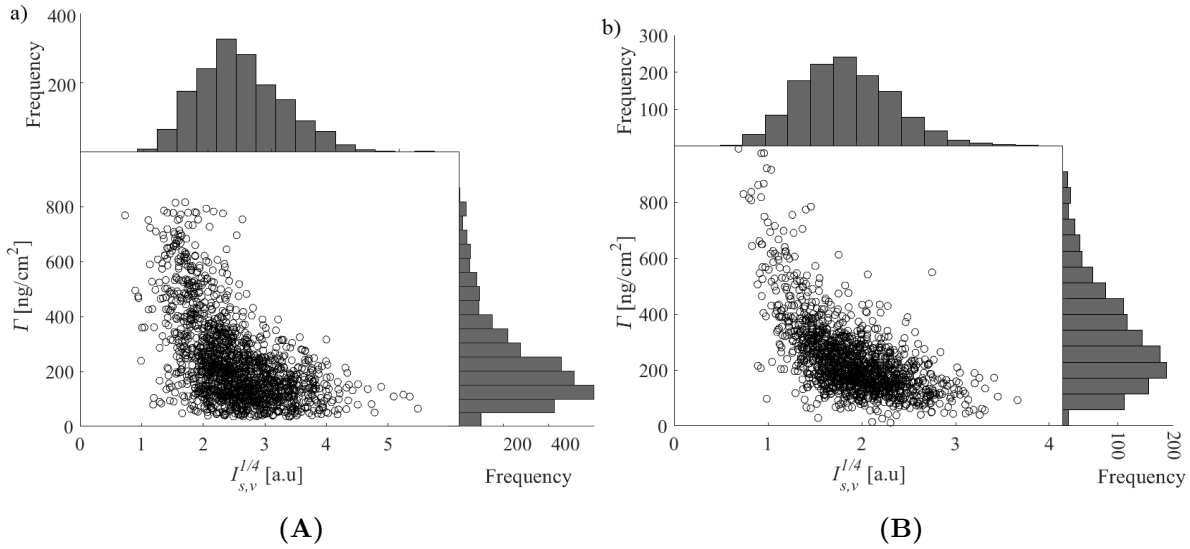

(A) **(B)**

Figure 5.3: Scatter plots of the calculated adsorbed protein surface concentration, Γ, as a function of the fourth root of the initial vesicle scattering intensity, which is proportional to the vesicle diameter, for a) streptavidin and b) anti-biotin binding to biotinylated vesicles, with the corresponding distributions projected onto the axes.

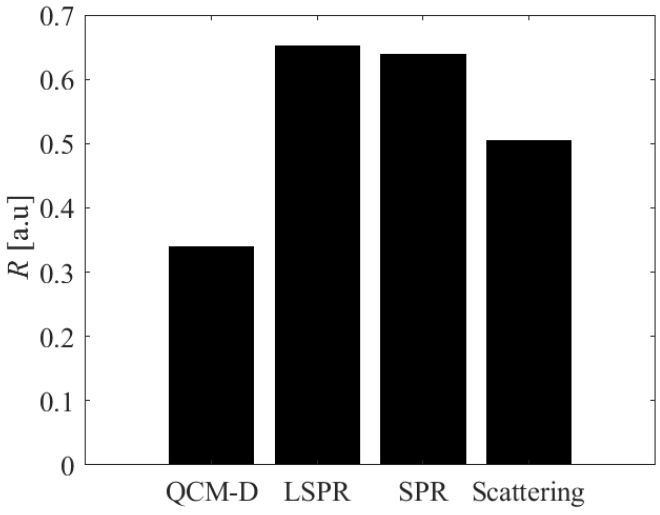

Figure 5.4: The response upon binding of streptavidin (CF488-SA) to biotinylated vesicles, as measured with QCM-D, LSPR, SPR and waveguide scattering microscopy. The responses are normalized to the prior vesicle binding response

in the bar plot should not be interpreted as less binding but highlights the fact of the significant contribution of coupled water, which is even higher for the hollow vesicles than for the proteins.

5.1.4 Conclusions

This study has demonstrated the possibility of utilizing waveguide scattering microscopy for mass quantification of protein binding to surface immobilized vesicles. The single particle resolution offered provides possibilities of sample subset identification and sensitivity levels orders of magnitude higher than ensemble average methods such as SPR. The method further allows for the exclusion of potential non-specific surface interactions, an advantage in comparison with the ensemble methods.

5.2 Paper II

This investigation utilizes two capabilities offered by dual-wavelength SPR, mass quantification and adherent thickness analysis, in order to elucidate the interplay between particle rigidity, ligand density and receptor distribution in a system modelling nanoparticle interactions with the cytosolic membrane. The system consists of liposomes binding to a supported lipid bilayer through the streptavidin-biotin interaction. The processes studied are of high interest in the context of for example pathogen recognition and initiation of cellular uptake pathways, where polyvalent interactions at the cell membrane is a central concept. Particle rigidity is expected to play a key roll in the cellular uptake process as the energy required for membrane envelopment of a highly deformable entity increases.

Two types of liposomes, consisting of either DOPC or DSPC as the main lipid and a fraction of DSPE-PEG(2000)-biotin, were studied while binding to biotinylated SLBs, saturated with streptavidin prior to the liposome addition (see figure 5.5 for an illustration of the experimental steps). The two liposomes, which at the experimental conditions used exhibited different lipid phase behavior, fluid- and gel phase for the DOPC and DSPC, respectively could be compared in terms of deformation upon interaction with the SLB.

As the liposomes were added to an SLB containing 0.5% biotinylated lipids, liposome coverage were in both cases below the expected jamming limit for random sequential adsorption of spheres to a planar surface ($\sim 54\%$), suggesting that the limiting factor for binding is not geometrical saturation of liposomes, but rather the amount of available ligands (streptavidin) on the SLB. This consequently means that all streptavidin are engaged in the binding of liposomes and thus are located in the liposome-SLB contact area. Based on the streptavidin and liposome masses measured, it was calculated that on average 100 and 56 streptavidin proteins per liposome for the fluid and gel phase liposomes, respectively. Using the interpretation approach outlined in section 4.2 the dimensions and thus the deformation and the contact area of the liposomes could be calculated (the fluid phase liposomes contracted from 105 nm to 90 nm while the gel phase liposome deformation was

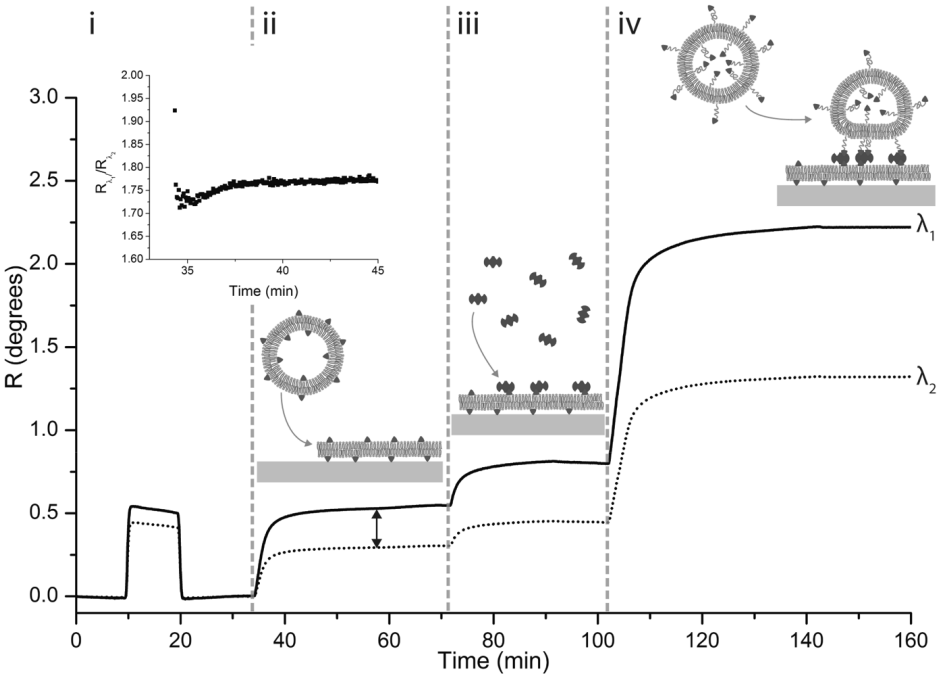

Figure 5.5: Illustration of a typical dual-wavelength SPR measurement with (i) injection of 5 wt% glycerol for calibration purposes, (ii) injection of liposomes and formation of an SLB containing 5 mol% cap biotin ($\Delta\Gamma \sim 345\,\mathrm{ng/cm^2}$), (iii) binding of SA ($\Delta\Gamma \sim 120\,\mathrm{ng/cm^2}$) and (iv) binding of DOPC-PEG-biotin ($\Delta\Gamma \sim 1100\,\mathrm{ng/cm^2}$, $d \sim 77\,\mathrm{nm}$). The inset shows the $R_{\lambda_1}/R_{\lambda_2}$ ratio upon SLB formation plotted vs time used to calibrate the decay lengths.

negligible) showing that the gel phase liposomes have significantly higher concentration of biotinylated lipids in the contact area than possible for immobile lipids, suggesting that the DSPE-PEG(2000)-biotin lipids are able to diffuse in the liposome bilayer in the gel phase liposomes as well as the fluid phase.

Adding the liposomes instead to an SLB containing 5% biotinylated lipids produced liposome coverages close to or above the jamming limit (for fluid and gel-phase liposomes, respectively), suggesting not only the expected possibility of bound liposomes to diffuse in the SLB surface but also that in the gel-phase case, steric hindrance due to reciprocal liposome interaction limits the amount of binding. In these cases liposome deformation from 105 nm to 75 nm and 93 nm for fluid and gel liposomes, respectively were observed. This corresponds to at least ~ 184 and ~ 79 streptavidin engaged in the respective cases, and possibly even higher. Hence, it appears likely that on the SLB, which served to mimic a cellular membrane, the liposome deformation of fluid-phase liposomes is limited by the number of available ligand-receptor bonds while membrane stiffness seems to play a significant role in limiting the deformation of gel-phase liposomes.

In conclusion, the possibility of investigating and potentially disentangling the effects of

nanoparticle deformation and interaction valency was demonstrated, while showing that differences in deformability seems to play an important role, worthy of further studies.

6

Future outlook

"Major rerum mihi nascitur ordo;
Majus opus moveo."

— Vergilius

The two papers presented here show the capabilities of waveguide scattering microscopy in combination with ensemble average methods such as SPR for sensitive studies and characterization of biological nanoparticles, so far illustrated by mass quantification of vesicle protein adhesion and surface induced vesicle deformation. Looking forwards, a main target is to move on from the model systems so far investigated and apply the methods for systems of higher complexity and more interest from an application perspective.

6.1 Opportunities for nanoparticle characterization

There is a range of entities and phenomena whose investigation could be aided by studies as those presented here. The diverse and currently important topic of nanoparticle-based drug delivery, including for example their use in ongoing vaccination trials against the COVID-19 pandemic[87, 88], faces a number of challenges which would be interesting to investigate.

The lipid nanoparticle delivery vehicle approach, briefly discussed in the biological background, is an intriguing route to transmembranal nucleic acid delivery. Single particle resolved observation of particles of this class, e.g. with respect to uptake of cargo or protein corona formation could potentially shed light on the complex task of effective utilization. As shown in paper I, the waveguide system has the opportunity of quantitative investigation of protein adherence to nanoparticles; extending its use to medically relevant particles, such as liposomal delivery systems[89] or lipid nanoparticles[90–92], and to more complex and relevant particle environments. For instance, by observing corona formation in serum, one would gain information on the distribution of coronal mass with respect to e.g. particle size, which combined with particle deformation analysis using SPR could

offer new insights regarding the ongoing effort of optimizing drug delivery vehicles with respect to its interactions with the protein corona. Beside lipid-based nanoparticles, similar studies, both of other delivery approaches and e.g. viruses are of high interest moving forwards.

Paper I claims the advantage of waveguide scattering microscopy compared to the other methods in terms of sensitivity with respect to amount of sample needed. A systematic series of measurements, further demonstrating this for biological systems available at low concentration would be of interest to conduct and compare with the capacity of e.g. SPR to offer the same information.

6.2 Waveguide development

The waveguide scattering microscopy platform used in this work has potential for further development. A property currently lacking is that of a simple and reliable system for handling controlled flow of sample over the waveguide chip surface. Implementation and utilization of a flow cell-based system is currently ongoing and will provide a significant addition to the system.

Another task ahead is the evaluation of the waveguide chip manufacturing process in order to optimize the fabrication and improve chip quality. There is currently a variation between individual chips in terms of unidentified scattering objects in the optical path, which might disturb parts of the measurement field of view. Identifying and eliminating the source of these will enable a smoother measurement and analysis process. A variation in chip facet quality also exists at the moment, with some chips having irregular edges which affects the coupling of light into the waveguide core. This would ideally be improved, likely with modification of the procedure of partitioning the produced wafer into individual chips.

Besides this, there is room for further developments in terms of choice of light sources and of waveguide core material for increasing the system sensitivity. The use of multiple illumination wavelengths is another interesting route, enabling the use of multiple fluorescent labels. This could be utilized e.g. for identifying protein corona components using secondary antibodies or distinguishing subclasses of extracellular vesicles through identification of expressed green fluorescent protein.

6.3 Data analysis

Machine learning algorithms is an interesting data analysis approach which may benefit studies as those presented here as it has often proven suitable for data noise reduction. I am personally intrigued by the potential opportunities of implementing machine learning algorithms for data analysis and investigate its applicability for identifying processes generating very low signals, where other methods of analysis are complicated. Investigating how far it is possible to push the sensitivity limits for the waveguide system, using novel

analysis methods, would definitely be interesting, and perhaps open up the use of this label-free method in diagnostic applications.

6.4 Particle rigidity and interaction valency

As demonstrated in paper II, both particle rigidity combined with high membrane fluidity seems to be beneficial in the context of cellular uptake. In order to further understand these processes, it would be interesting to use samples where these two parameters are fully decoupled and can be studies separately. A possible route to this would be to use rigid nanoparticles coated with a fluid lipid bilayer, rather than with liposomes.

Acknowledgements

I would like to express my gratitude to everyone which in one way or another has contributed to this thesis.

Fredrik Höök, my main supervisor. I really appreciate your style of supervising. Thanks for all insightful comments, guidance and help.

Björn Agnarsson and ***Antonius Armanious***, my co-supervisors. Thanks for all our discussions on experiments and data interpretation. For the many great suggestions which has helped moving this project forwards.

Co-authors. Thanks for good cooperation. I hope we can continue collaborating in the future. A special thanks to ***Karin Norling*** for good collaboration on paper II, and to ***Mokhtar Mapar*** for all your help with the waveguide.

Adrián González Rodríguez and ***Erik Olsén***. Thanks for helping me proofreading this thesis and for our many discussions on everything from biophysics to AI-apocalypse scenarios.

Past and present members of the ***Biological Physics group***. Thanks for good cooperation, interesting fika-discussions and a stimulating, friendly and welcoming working environment. A special thanks to my (past and present) ***Office mates*** for making work fun more often than not.

My family and friends, for being just that.

Soli Deo Gloria.

Mattias Sjöberg, Göteborg, July 2020

Bibliography

[1] R. Hooke, *Micrographia*. LONDON, Printed by Jo. Martyn, and Ja. Allestry, Printers to the Royal Society, and are to be sold at their Shop at the Bell in S. Paul's Churchyard. M DC LX V., 1665.

[2] H. Lodish, A. Berk, S. L. Zipursky, P. Matsudaira, D. Baltimore, and J. Darnell, "Microscopy and cell architecture," in *Molecular Cell Biology. 8th edition*, WH Freeman, 2016.

[3] B. E. Rapp, F. J. Gruhl, and K. Länge, "Biosensors with label-free detection designed for diagnostic applications," *Analytical and bioanalytical chemistry*, vol. 398, no. 6, pp. 2403–2412, 2010.

[4] S. Stanley, "Biological nanoparticles and their influence on organisms," *Current opinion in biotechnology*, vol. 28, pp. 69–74, 2014.

[5] E. Blanco, H. Shen, and M. Ferrari, "Principles of nanoparticle design for overcoming biological barriers to drug delivery," *Nature biotechnology*, vol. 33, no. 9, p. 941, 2015.

[6] M. Tkach and C. Théry, "Communication by extracellular vesicles: where we are and where we need to go," *Cell*, vol. 164, no. 6, pp. 1226–1232, 2016.

[7] R. E. Veerman, G. G. Akpinar, M. Eldh, and S. Gabrielsson, "Immune cell-derived extracellular vesicles–functions and therapeutic applications," *Trends in molecular medicine*, 2019.

[8] K. W. Witwer, E. I. Buzás, L. T. Bemis, A. Bora, C. Lässer, J. Lötvall, E. N. Nolte-'t Hoen, M. G. Piper, S. Sivaraman, J. Skog, *et al.*, "Standardization of sample collection, isolation and analysis methods in extracellular vesicle research," *Journal of extracellular vesicles*, vol. 2, no. 1, p. 20360, 2013.

[9] S. L. Maas, X. O. Breakefield, and A. M. Weaver, "Extracellular vesicles: unique intercellular delivery vehicles," *Trends in cell biology*, vol. 27, no. 3, pp. 172–188, 2017.

[10] B. Pelaz, C. Alexiou, R. A. Alvarez-Puebla, F. Alves, A. M. Andrews, S. Ashraf, L. P. Balogh, L. Ballerini, A. Bestetti, C. Brendel, *et al.*, "Diverse applications of nanomedicine," 2017.

[11] P. Vader, E. A. Mol, G. Pasterkamp, and R. M. Schiffelers, "Extracellular vesicles for drug delivery," *Advanced drug delivery reviews*, vol. 106, pp. 148–156, 2016.

[12] R. Kanasty, J. R. Dorkin, A. Vegas, and D. Anderson, "Delivery materials for sirna therapeutics," *Nature materials*, vol. 12, no. 11, pp. 967–977, 2013.

[13] D. W. Bartlett and M. E. Davis, "Physicochemical and biological characterization of targeted, nucleic acid-containing nanoparticles," *Bioconjugate chemistry*, vol. 18, no. 2, pp. 456–468, 2007.

[14] P. J. Lin, Y. K. Tam, and P. R. Cullis, "Development and clinical applications of sirna-encapsulated lipid nanoparticles in cancer," *Clinical Lipidology*, vol. 9, no. 3, pp. 317–331, 2014.

[15] D. Docter, D. Westmeier, M. Markiewicz, S. Stolte, S. Knauer, and R. Stauber, "The nanoparticle biomolecule corona: lessons learned–challenge accepted?," *Chemical Society Reviews*, vol. 44, no. 17, pp. 6094–6121, 2015.

[16] M. Mammen, S.-K. Choi, and G. M. Whitesides, "Polyvalent interactions in biological systems: implications for design and use of multivalent ligands and inhibitors," *Angewandte Chemie International Edition*, vol. 37, no. 20, pp. 2754–2794, 1998.

[17] H. Metzger, "Transmembrane signaling: the joy of aggregation.," *The Journal of Immunology*, vol. 149, no. 5, pp. 1477–1487, 1992.

[18] L. I. Conrad, M. Neve, V. Nutton, R. Porter, and A. Wear, *The Western medical tradition: 800 BC to AD 1800*, vol. 1. Cambridge University Press, 1995.

[19] G. Ehud and M. Anna, *Plenty of room for biology at the bottom: an introduction to bionanotechnology*. World Scientific, 2013.

[20] M.-X. Wu and Y.-W. Yang, "Metal–organic framework (mof)-based drug/cargo delivery and cancer therapy," *Advanced Materials*, vol. 29, no. 23, p. 1606134, 2017.

[21] J. G. Croissant, Y. Fatieiev, A. Almalik, and N. M. Khashab, "Mesoporous silica and organosilica nanoparticles: physical chemistry, biosafety, delivery strategies, and biomedical applications," *Advanced healthcare materials*, vol. 7, no. 4, p. 1700831, 2018.

[22] R. Rupaimoole and F. J. Slack, "Microrna therapeutics: towards a new era for the management of cancer and other diseases," *Nature reviews Drug discovery*, vol. 16, no. 3, p. 203, 2017.

[23] J. Shi, P. W. Kantoff, R. Wooster, and O. C. Farokhzad, "Cancer nanomedicine: progress, challenges and opportunities," *Nature Reviews Cancer*, vol. 17, no. 1, p. 20, 2017.

[24] L. Wang, C. Hu, and L. Shao, "The antimicrobial activity of nanoparticles: present situation and prospects for the future," *International journal of nanomedicine*, vol. 12, p. 1227, 2017.

[25] R. Kalluri and V. S. LeBleu, "The biology, function, and biomedical applications of exosomes," *Science*, vol. 367, no. 6478, 2020.

[26] A. E. Czapar and N. F. Steinmetz, "Plant viruses and bacteriophages for drug delivery in medicine and biotechnology," *Current opinion in chemical biology*, vol. 38, pp. 108–116, 2017.

[27] R. Phillips, J. Kondev, J. Theriot, and H. Garcia, *Physical biology of the cell*. Garland Science, 2012.

[28] B. S. Pattni, V. V. Chupin, and V. P. Torchilin, "New developments in liposomal drug delivery," *Chemical reviews*, vol. 115, no. 19, pp. 10938–10966, 2015.

[29] T. P. Prakash, M. J. Graham, J. Yu, R. Carty, A. Low, A. Chappell, K. Schmidt, C. Zhao, M. Aghajan, H. F. Murray, *et al.*, "Targeted delivery of antisense oligonucleotides to hepatocytes using triantennary n-acetyl galactosamine improves potency 10-fold in mice," *Nucleic acids research*, vol. 42, no. 13, pp. 8796–8807, 2014.

[30] G. Walsh, "Pharmaceuticals, biologics and biopharmaceuticals," *Biopharmaceuticals: Biochemistry and Biotechnology, 2nd ed. John Wiley & Sons, Inc., Hoboken, NJ*, 2003.

[31] H. Lodish, A. Berk, C. A. Kaiser, M. Krieger, M. P. Scott, A. Bretscher, H. Ploegh, P. Matsudaira, *et al.*, *Molecular cell biology*. Macmillan, 2008.

[32] J. Nissen, S. Gritsch, G. Wiegand, and J. Rädler, "Wetting of phospholipid membranes on hydrophilic surfaces-concepts towards self-healing membranes," *The European Physical Journal B-Condensed Matter and Complex Systems*, vol. 10, no. 2, pp. 335–344, 1999.

[33] W. Rawicz, K. C. Olbrich, T. McIntosh, D. Needham, and E. Evans, "Effect of chain length and unsaturation on elasticity of lipid bilayers," *Biophysical journal*, vol. 79, no. 1, pp. 328–339, 2000.

[34] I. Pfeiffer and F. Höök, "Bivalent cholesterol-based coupling of oligonucletides to lipid membrane assemblies," *Journal of the American Chemical Society*, vol. 126, no. 33, pp. 10224–10225, 2004.

[35] M. Hope, M. Bally, G. Webb, and P. Cullis, "Production of large unilamellar vesicles by a rapid extrusion procedure. characterization of size distribution, trapped volume and ability to maintain a membrane potential," *Biochimica et Biophysica Acta (BBA)-Biomembranes*, vol. 812, no. 1, pp. 55–65, 1985.

[36] S. G. M. Ong, M. Chitneni, K. S. Lee, L. C. Ming, and K. H. Yuen, "Evaluation of extrusion technique for nanosizing liposomes," *Pharmaceutics*, vol. 8, no. 4, p. 36, 2016.

[37] C. Corbo, R. Molinaro, A. Parodi, N. E. Toledano Furman, F. Salvatore, and E. Tasciotti, "The impact of nanoparticle protein corona on cytotoxicity, immunotoxicity and target drug delivery," *Nanomedicine*, vol. 11, no. 1, pp. 81–100, 2016.

[38] M. P. Monopoli, D. Walczyk, A. Campbell, G. Elia, I. Lynch, F. Baldelli Bombelli, and K. A. Dawson, "Physical- chemical aspects of protein corona: relevance to in vitro and in vivo biological impacts of nanoparticles," *Journal of the American Chemical Society*, vol. 133, no. 8, pp. 2525–2534, 2011.

[39] C. D. Walkey and W. C. Chan, "Understanding and controlling the interaction of nanomaterials with proteins in a physiological environment," *Chemical Society Reviews*, vol. 41, no. 7, pp. 2780–2799, 2012.

[40] S. Wan, P. M. Kelly, E. Mahon, H. Stockmann, P. M. Rudd, F. Caruso, K. A. Dawson, Y. Yan, and M. P. Monopoli, "The "sweet" side of the protein corona: effects of glycosylation on nanoparticle–cell interactions," *ACS nano*, vol. 9, no. 2, pp. 2157–2166, 2015.

[41] E. Hellstrand, I. Lynch, A. Andersson, T. Drakenberg, B. Dahlbäck, K. A. Dawson, S. Linse, and T. Cedervall, "Complete high-density lipoproteins in nanoparticle corona," *The FEBS journal*, vol. 276, no. 12, pp. 3372–3381, 2009.

[42] S. Milani, F. Baldelli Bombelli, A. S. Pitek, K. A. Dawson, and J. Radler, "Reversible versus irreversible binding of transferrin to polystyrene nanoparticles: soft and hard corona," *ACS nano*, vol. 6, no. 3, pp. 2532–2541, 2012.

[43] E. Casals, T. Pfaller, A. Duschl, G. J. Oostingh, and V. Puntes, "Time evolution of the nanoparticle protein corona," *ACS nano*, vol. 4, no. 7, pp. 3623–3632, 2010.

[44] D. Docter, U. Distler, W. Storck, J. Kuharev, D. Wünsch, A. Hahlbrock, S. K. Knauer, S. Tenzer, and R. H. Stauber, "Quantitative profiling of the protein coronas that form around nanoparticles," *Nature protocols*, vol. 9, no. 9, pp. 2030–2044, 2014.

[45] O. K. Kari, J. Ndika, P. Parkkila, A. Louna, T. Lajunen, A. Puustinen, T. Viitala, H. Alenius, and A. Urtti, "In situ analysis of liposome hard and soft protein corona structure and composition in a single label-free workflow," *Nanoscale*, vol. 12, no. 3, pp. 1728–1741, 2020.

[46] D. Di Silvio, M. Maccarini, R. Parker, A. Mackie, G. Fragneto, and F. B. Bombelli, "The effect of the protein corona on the interaction between nanoparticles and lipid bilayers," *Journal of colloid and interface science*, vol. 504, pp. 741–750, 2017.

[47] T. Cedervall, I. Lynch, S. Lindman, T. Berggård, E. Thulin, H. Nilsson, K. A. Dawson, and S. Linse, "Understanding the nanoparticle–protein corona using methods to quantify exchange rates and affinities of proteins for nanoparticles," *Proceedings of the National Academy of Sciences*, vol. 104, no. 7, pp. 2050–2055, 2007.

[48] O. K. Kari, T. Rojalin, S. Salmaso, M. Barattin, H. Jarva, S. Meri, M. Yliperttula, T. Viitala, and A. Urtti, "Multi-parametric surface plasmon resonance platform for studying liposome-serum interactions and protein corona formation," *Drug delivery and translational research*, vol. 7, no. 2, pp. 228–240, 2017.

[49] G. C. Brittain, Y. Q. Chen, E. Martinez, V. A. Tang, T. M. Renner, M.-A. Langlois, and S. Gulnik, "A novel semiconductor-based flow cytometer with enhanced light-scatter sensitivity for the analysis of biological nanoparticles," *Scientific reports*, vol. 9, no. 1, pp. 1–13, 2019.

[50] N. M. Green, "Avidin," in *Advances in protein chemistry*, vol. 29, pp. 85–133, Elsevier, 1975.

[51] R. Feynman, R. Leighton, and M. Sands, *The Feynman Lectures on Physics, Vol II: Commemorative Issue*. Addison-Wesley, 1989.

[52] E. Hecht, *Optics*. Pearson Education, Incorporated, 2017.

[53] L. Novotny and B. Hecht, *Principles of Nano-Optics*. Cambridge University Press, 2006.

[54] C. Bohren and D. Huffman, *Absorption and Scattering of Light by Small Particles*. Wiley Science Series, Wiley, 2008.

[55] H. Zhao, P. H. Brown, and P. Schuck, "On the distribution of protein refractive index increments," *Biophysical journal*, vol. 100, no. 9, pp. 2309–2317, 2011.

[56] J. De Feijter, d. J. Benjamins, and F. Veer, "Ellipsometry as a tool to study the adsorption behavior of synthetic and biopolymers at the air–water interface," *Biopolymers: Original Research on Biomolecules*, vol. 17, no. 7, pp. 1759–1772, 1978.

[57] R. B. Miles, W. R. Lempert, and J. N. Forkey, "Laser rayleigh scattering," *Measurement Science and Technology*, vol. 12, no. 5, p. R33, 2001.

[58] L. Rayleigh, "On the electromagnetic theory of light," *The London, Edinburgh, and Dublin Philosophical Magazine and Journal of Science*, vol. 12, no. 73, pp. 81–101, 1881.

[59] B. Agnarsson, A. Lundgren, A. Gunnarsson, M. Rabe, A. Kunze, M. Mapar, L. Simonsson, M. Bally, V. P. Zhdanov, and F. Höök, "Evanescent light-scattering microscopy for label-free interfacial imaging: from single sub-100 nm vesicles to live cells," *ACS nano*, vol. 9, no. 12, pp. 11849–11862, 2015.

[60] J. K. Hannestad, S. Rocha, B. Agnarsson, V. P. Zhdanov, P. Wittung-Stafshede, and F. Höök, "Single-vesicle imaging reveals lipid-selective and stepwise membrane disruption by monomeric α-synuclein," *Proceedings of the National Academy of Sciences*, 2020.

[61] D. Axelrod, "Cell-substrate contacts illuminated by total internal reflection fluorescence.," *Journal of Cell Biology*, vol. 89, no. 1, pp. 141–145, 1981.

[62] D. K. Cheng *et al.*, *Field and wave electromagnetics*. Pearson Education India, 1989.

[63] J. R. Lakowicz, *Principles of fluorescence spectroscopy*. Springer science & business media, 2013.

[64] D. Axelrod, E. H. Hellen, and R. M. Fulbright, "Total internal reflection fluorescence," in *Topics in fluorescence spectroscopy*, pp. 289–343, Springer, 2002.

[65] K. Leosson and B. Agnarsson, "Integrated biophotonics with cytop," *Micromachines*, vol. 3, no. 1, pp. 114–125, 2012.

[66] B. Agnarsson, S. Ingthorsson, T. Gudjonsson, and K. Leosson, "Evanescent-wave fluorescence microscopy using symmetric planar waveguides," *Optics express*, vol. 17, no. 7, pp. 5075–5082, 2009.

[67] B. Agnarsson, M. Mapar, M. Sjöberg, M. Alizadehheidari, and F. Höök, "Low-temperature fabrication and characterization of a symmetric hybrid organic–inorganic slab waveguide for evanescent light microscopy," *Nano Futures*, vol. 2, no. 2, p. 025007, 2018.

[68] A. B. Dahlin, *Plasmonic biosensors: an integrated view of refractometric detection*, vol. 4. Ios Press, 2012.

[69] S. A. Maier, *Plasmonics: fundamentals and applications*. Springer Science & Business Media, 2007.

[70] D. Barber and I. C. Freestone, "An investigation of the origin of the colour of the lycurgus cup by analytical transmission electron microscopy," *Archaeometry*, vol. 32, no. 1, pp. 33–45, 1990.

[71] E. Kretschmann and H. Raether, "Radiative decay of non radiative surface plasmons excited by light," *Zeitschrift für Naturforschung A*, vol. 23, no. 12, pp. 2135–2136, 1968.

[72] A. Otto, "Excitation of nonradiative surface plasma waves in silver by the method of frustrated total reflection," *Zeitschrift für Physik A Hadrons and nuclei*, vol. 216, no. 4, pp. 398–410, 1968.

[73] B. Liedberg, C. Nylander, and I. Lunström, "Surface plasmon resonance for gas detection and biosensing," *Sensors and actuators*, vol. 4, pp. 299–304, 1983.

[74] J. Homola and M. Piliarik, "Surface plasmon resonance (spr) sensors," in *Surface plasmon resonance based sensors*, pp. 45–67, Springer, 2006.

[75] L. S. Jung, C. T. Campbell, T. M. Chinowsky, M. N. Mar, and S. S. Yee, "Quantitative interpretation of the response of surface plasmon resonance sensors to adsorbed films," *Langmuir*, vol. 14, no. 19, pp. 5636–5648, 1998.

[76] D. L. Rupert, C. Lässer, M. Eldh, S. Block, V. P. Zhdanov, J. O. Lotvall, M. Bally, and F. Höök, "Determination of exosome concentration in solution using surface plasmon resonance spectroscopy," *Analytical chemistry*, vol. 86, no. 12, pp. 5929–5936, 2014.

[77] D. L. Rupert, G. V. Shelke, G. Emilsson, V. Claudio, S. Block, C. Lässer, A. Dahlin, J. O. Lötvall, M. Bally, V. P. Zhdanov, and F. Höök, "Dual-Wavelength Surface Plasmon Resonance for Determining the Size and Concentration of Sub-Populations of Extracellular Vesicles," *Analytical Chemistry*, vol. 88, no. 20, pp. 9980–9988, 2016.

[78] G. E. Perlmann and L. Longsworth, "The specific refractive increment of some purified proteins," *Journal of the American Chemical Society*, vol. 70, no. 8, pp. 2719–2724, 1948.

[79] A. Dmitriev, *Nanoplasmonic sensors*. Springer Science & Business Media, 2012.

[80] A. J. Haes and R. P. Van Duyne, "A unified view of propagating and localized surface plasmon resonance biosensors," *Analytical and bioanalytical chemistry*, vol. 379, no. 7-8, pp. 920–930, 2004.

[81] G. Sauerbrey, "Verwendung von schwingquarzen zur wägung dünner schichten und zur mikrowägung," *Zeitschrift für physik*, vol. 155, no. 2, pp. 206–222, 1959.

[82] A. Janshoff, H.-J. Galla, and C. Steinem, "Piezoelectric mass-sensing devices as biosensors—an alternative to optical biosensors?," *Angewandte Chemie International Edition*, vol. 39, no. 22, pp. 4004–4032, 2000.

[83] S.-Z. Yao and T.-A. Zhou, "Dependence of the oscillation frequency of a piezoelectric crystal on the physical parameters of liquids," *Analytica chimica acta*, vol. 212, pp. 61–72, 1988.

[84] E. Nilebäck, *QCM-D–with focus on biosensing in biomolecular and cellular systems*. Chalmers University of Technology, 2013.

[85] F. Höök, B. Kasemo, T. Nylander, C. Fant, K. Sott, and H. Elwing, "Variations in coupled water, viscoelastic properties, and film thickness of a mefp-1 protein film during adsorption and cross-linking: a quartz crystal microbalance with dissipation monitoring, ellipsometry, and surface plasmon resonance study," *Analytical chemistry*, vol. 73, no. 24, pp. 5796–5804, 2001.

[86] J. DeChancie and K. Houk, "The origins of femtomolar protein- ligand binding: hydrogen-bond cooperativity and desolvation energetics in the biotin-(strept) avidin binding site," *Journal of the American Chemical Society*, vol. 129, no. 17, pp. 5419–5429, 2007.

[87] C. Weiss, M. Carriere, L. Fusco, I. Capua, J. A. Regla-Nava, M. Pasquali, J. A. Scott, F. Vitale, M. A. Unal, C. Mattevi, *et al.*, "Toward nanotechnology-enabled approaches against the covid-19 pandemic," *ACS Nano*, 2020.

[88] F. Wang, R. M. Kream, and G. B. Stefano, "An evidence based perspective on mrna-sars-cov-2 vaccine development," *Medical Science Monitor: International Medical Journal of Experimental and Clinical Research*, vol. 26, pp. e924700–1, 2020.

[89] L. Sercombe, T. Veerati, F. Moheimani, S. Y. Wu, A. K. Sood, and S. Hua, "Advances and challenges of liposome assisted drug delivery," *Frontiers in pharmacology*, vol. 6, p. 286, 2015.

[90] H. M. Barriga, M. N. Holme, and M. M. Stevens, "Cubosomes: the next generation of smart lipid nanoparticles?," *Angewandte Chemie International Edition*, vol. 58, no. 10, pp. 2958–2978, 2019.

[91] M. Maugeri, M. Nawaz, A. Papadimitriou, A. Angerfors, A. Camponeschi, M. Na, M. Hölttä, P. Skantze, S. Johansson, M. Sundqvist, *et al.*, "Linkage between endosomal escape of lnp-mrna and loading into evs for transport to other cells," *Nature communications*, vol. 10, no. 1, pp. 1–15, 2019.

[92] S. Patel, N. Ashwanikumar, E. Robinson, A. DuRoss, C. Sun, K. E. Murphy-Benenato, C. Mihai, O. Almarsson, and G. Sahay, "Boosting intracellular delivery of lipid nanoparticle-encapsulated mrna," *Nano letters*, vol. 17, no. 9, pp. 5711–5718, 2017.